DISSERTATIONES
SCIENTIAE
MATERIALIS
UNIVERSITATIS
TARTUENSIS
**38**

ARTJOM BERHOLTS

# Light-enhanced sensors of oxidizing gases based on single-layer CVD graphene

DISSERTATIONES SCIENTIAE MATERIALIS UNIVERSITATIS TARTUENSIS
**38**

DISSERTATIONES SCIENTIAE MATERIALIS UNIVERSITATIS TARTUENSIS
**38**

**ARTJOM BERHOLTS**

# Light-enhanced sensors of oxidizing gases based on single-layer CVD graphene

UNIVERSITY OF TARTU
Press
1632

The study was carried out at the Institute of Physics, University of Tartu, Estonia.

The Dissertation was admitted on September 25, 2024, in partial fulfillment of the requirements for the degree of Doctor of Philosophy in Material Science, and allowed for defense by the Scientific Council on Material Science of the Faculty of Science and Technology of the University of Tartu.

Supervisors: Raivo Jaaniso, Institute of Physics, University of Tartu

Harry Alles, Institute of Physics, University of Tartu

Opponents: Prof. Krisztián Kordás, University of Oulu

Commencement: November 20, 2024 at University of Tartu, Tartu, Estonia

This work has been partially supported by the Estonian Research Council (grants PRG753, PRG1580, IUT34-27, IUT2-24), European Social Fund (Grant MTT1) and via the European Union's Horizon 2020 research and innovation program under Graphene Flagship grant agreements No. 696656 and No. 881603.

ISSN 2228-0928 (print)
ISBN 978-9916-27-704-1 (print)
ISSN 2806-2574 (pdf)
ISBN 978-9916-27-705-8 (pdf)

Copyright: Artjom Berholts, 2024

University of Tartu Press
www.tyk.ee

# TABLE OF CONTENTS

LIST OF ORIGINAL PUBLICATIONS AND AUTHOR'S CONTRIBUTIONS ..... 6

LIST OF ABBREVIATIONS ..... 7

THE CLAIM OF THE THESIS ..... 8

1. INTRODUCTION ..... 9

2. BACKGROUND ..... 11
   2.1 Graphene ..... 11
      2.1.1 Graphene structure and properties ..... 11
      2.1.2 Electronic properties of graphene ..... 12
      2.1.3 Production of graphene ..... 13
   2.2 Gas sensors ..... 14
      2.2.1 Key characteristics ..... 14
      2.2.2 Graphene as a gas sensor ..... 15

3. EXPERIMENTAL GOALS AND THE STRUCTURE OF THE STUDY ..... 19

4. EXPERIMENTAL DETAILS ..... 20
   4.1 Sensor preparation ..... 20
   4.2 Experimental setup ..... 21
   4.3 Characterization techniques ..... 23

5. RESULTS ..... 24
   5.1 Pristine graphene ..... 24
   5.2 Graphene functionalized with $ZrO_2$ and Ag ..... 29
   5.3 Graphene/$TiO_2$ heterostructures ..... 34

6. CONCLUSIONS ..... 47

SUMMARY IN ESTONIAN ..... 49

ACKNOWLEDGEMENTS ..... 51

REFERENCES ..... 52

ORIGINAL PUBLICATIONS ..... 61

CURRICULUM VITAE ..... 92

ELULOOKIRJELDUS ..... 94

# LIST OF ORIGINAL PUBLICATIONS AND AUTHOR'S CONTRIBUTIONS

This thesis is based on the following publications:

**I**. **Berholts, A**., Kahro, T., Floren, A., Alles, H., Jaaniso, R., Photo-activated oxygen sensitivity of graphene at room temperature, *Appl. Phys. Lett.*, 105, 163111/1–5 (2014).

The author measured the electrical characteristics and gas sensitivity of graphene and analyzed the results. He also conducted the measurements of field effect transistor characteristics and prepared the figures for the manuscript as well as the part of the text concerning gas sensing measurements.

**II**. Kodu, M., **Berholts, A**., Kahro, T., Avarmaa, T., Kasikov, A., Niilisk, A., Alles, H., Jaaniso R., Highly sensitive $NO_2$ sensors by pulsed laser deposition on graphene, *Appl. Phys. Lett.*, 109, 113108/1–5 (2016).

The author was responsible for the measurement of graphene's electrical characteristics and gas sensitivity and carried out the analysis of the results. He also participated in the Raman measurements and prepared the figures for the manuscript.

**III**. **Berholts, A**., Kodu, M., Rubin, P., Kahro, T., Alles, H., Jaaniso, R., Layered Heterostructure of Graphene and $TiO_2$ as a Highly Sensitive and Stable Photoassisted $NO_2$ Sensor, *ACS Appl. Mater. Interfaces*, 16 (33), 43827–43837 (2024).

The author's responsibility was to measure electrical characteristics and gas sensitivity of graphene, together with the analysis of the results. He participated in Raman measurements and conducted the measurements of field effect transistor characteristics. The author also wrote the original draft of the manuscript.

# LIST OF ABBREVIATIONS

| | | |
|---|---|---|
| 2D | – | two-dimensional |
| CNT | – | carbon nanotubes |
| CVD | – | chemical vapor deposition |
| FLG | – | few-layer graphene |
| Gr | – | graphene |
| LOD | – | limit of detection |
| PLD | – | pulsed laser deposition |
| PMMA | – | poly(methyl methacrylate) |
| ppb | – | parts per billion |
| ppm | – | parts per million |
| rGO | – | reduced graphene oxide |
| RH | – | relative humidity |
| SEM | – | scanning electron microscopy |
| SLG | – | single-layer graphene |
| SMOX | – | semiconducting metal oxide |
| UHV | – | ultra high vacuum |
| UV | – | ultraviolet |
| VOC | – | volatile organic compound |
| XRF | – | X-ray fluorescence |
| XPS | – | X-ray photoelectron spectroscopy |

# THE CLAIM OF THE THESIS

Gas sensing properties of both pristine and PLD-modified graphene could be improved via UV light irradiation. UV light is capable of cleaning the surface of graphene from the environmental adsorbates as well as speeding up the response and recovery kinetics of the gas sensors. Together with the optimized functionalization this could pave the way for a new class of gas sensors based on two-dimensional heterostructures.

# 1. INTRODUCTION

Gas sensors are devices with the primary function of detecting and identifying the presence of a target gas in a certain area. They are often an integral part of the safety systems that evaluate the potential risks to human health and industrial equipment. The primary detection mechanism of the chemiresistive gas sensors involves the adsorption of gas species on the material's surface. Graphene, being a one-atom-thick two-dimensional material, emerges as an ultimate gas sensor building block for it. The entire surface of graphene can be effectively utilized for gas adsorption.

Graphene was first successfully isolated from graphite flakes using micromechanical exfoliation about 20 years ago [1]. Since then numerous production methods have been developed, aiming to achieve a scalable production of high-quality graphene sheets, including chemical vapor deposition (CVD) [2]. Graphene and other carbon-based materials, like carbon nanotubes (CNT), have been investigated as a potential replacement for the traditionally used gas sensors based on semiconductor metal oxides (SMOX) [3], with a goal of achieving lower device operating temperatures, extending the lifespan of the sensors and improving their selectivity.

It should be noted that pristine CVD graphene is normally too inert to effectively work as a gas sensor under ambient conditions at room temperature [4–7], partially because there is a high chance that the contaminants such as water vapor or volatile organic compounds could adsorb onto graphene from the environment and passivate its surface. UV light can assist with surface cleaning and enhance sensor performance [8, 9], similar to the heating effect in the case of SMOX gas sensors. Additionally, the functionalization of graphene could help it reach its full potential as a gas sensor, enhancing the adsorption properties of the material [10]. Deposited additives and defects serve as adsorption centers for target gas molecules, leading to increased charge transfer [11]. The pulsed laser deposition (PLD) method provides controlled deposition of a wide variety of materials, including metals, oxides, semiconductors, and nitrides [12]. An appropriate choice of functionalizing groups enables the sensor to be tuned towards the detection of a specific gas [13]. UV light might also have a great synergy with materials used to functionalize graphene, such as Ag, $ZrO_2$, and $TiO_2$, via the excitations due to the light absorption in the dopants.

A wide variety of gases originating both from natural and anthropogenic sources requires continuous monitoring. Gas pollutants, like $NO_2$, CO, $SO_2$ and others, pose health risks for humans when gas concentrations exceed safety limits. $NO_2$, for instance, could be the cause of airway inflammation and respiratory disorders, including asthma [14, 15]. Gas cooking stoves, cigarettes and motor vehicles are the common human-caused sources of $NO_2$. The annual $NO_2$ mean value recommended by WHO is 10 $\mu g/m^3$, with EU (40 $\mu g/m^3$) and US (100 $\mu g/m^3$) limits being slightly higher [16]. $NO_2$ is only one of the examples of gases that might endanger human life. The existence of colorless, odorless, and tasteless toxic gases

like CO, which the human body cannot directly detect [17], underlines the critical necessity for the development and deployment of reliable and precise gas sensors.

The main goal of this thesis was to investigate and characterize graphene-based sensors at room temperature and study the light illumination effect on the gas sensing parameters, starting from pristine single-layer CVD graphene on $Si/SiO_2$ substrate (**Paper I**), followed by the functionalization of CVD graphene with $ZrO_2$ and Ag (**Paper II**) and $TiO_2$ (**Paper III**) using PLD method.

# 2. BACKGROUND

## 2.1 Graphene

### 2.1.1 Graphene structure and properties

Carbon has an electronic configuration of $1s^2 2s^2 2p^2$, with four electrons available for bond formation. This allows carbon to form stable $sp^3$ hybrids (diamond), $sp^1$ hybrids (acetylene) or $sp^2$ hybrids like benzene and graphene [18]. Graphene, specifically, is a monolayer composed of $sp^2$ hybridized carbon atoms arranged in a hexagonal lattice. The in-plane σ-bonds are at a 120° angle to each other. Schematic of the hexagonal lattice of graphene on top of a substrate is demonstrated in Figure 1. Due to the predictions that a single graphene sheet would be thermodynamically unstable, isolating free-standing graphene sheets seemed implausible until in 2004, in Manchester, Geim's group succeeded at separating small graphene flakes from graphite using the micromechanical cleavage method [1]. Multiple methods of graphene growth have been developed since then, and those are discussed in one of the subsequent sections.

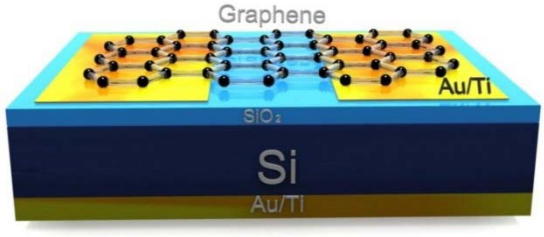


**Figure 1**. Hexagonal graphene lattice on top of $Si/SiO_2$ substrate with Au/Ti contacts. Reproduced from **Paper I** with the permission of AIP Publishing.

Graphene is a suitable material for flexible electronics, as it maintains its shape under stress; the graphene sheet also demonstrates a good chemical resistance and thermal stability. Despite being a one atom-layer-thick material, graphene exhibits remarkable impermeability to gas [19] and its optical transmittance could reach up to 97.7% [20].

Graphene has excellent mechanical properties (tensile strength, 130 GPa) due to the 0.142 nm long carbon-carbon bond [19]. Besides being one of the strongest materials discovered, it is also extremely light as the density of graphene is only 0.76 $mg/m^2$. Graphene is a good thermal conductor as well, with room temperature in-plane conductivity reaching 3000–5000 $W \cdot m^{-1} \cdot K^{-1}$, which is higher than diamond (2000 $W \cdot m^{-1} \cdot K^{-1}$) and CNT (3000 $W \cdot m^{-1} \cdot K^{-1}$) [21].

### 2.1.2 Electronic properties of graphene

The remarkable electronic properties of graphene are one of the reasons why this material attracted so much attention in the last couple of decades. A carbon atom, with an electronic configuration of $1s^2 2s^2 2p^2$, possesses a total of 6 electrons – 2 in an inner shell and 4 in an outer shell [22]. In graphene, three strong covalent σ bonds are formed in a two-dimensional *xy*-plane by 3 outer shell electrons [22]. Those σ-bonds connect each carbon atom with its three closest neighboring carbon atoms. The remaining free electron in the outer shell, known as π-electron, contributes to the electrical conductance of graphene and forms a π-bond located above or below graphene's two-dimensional structure (*z*-axis) [22].

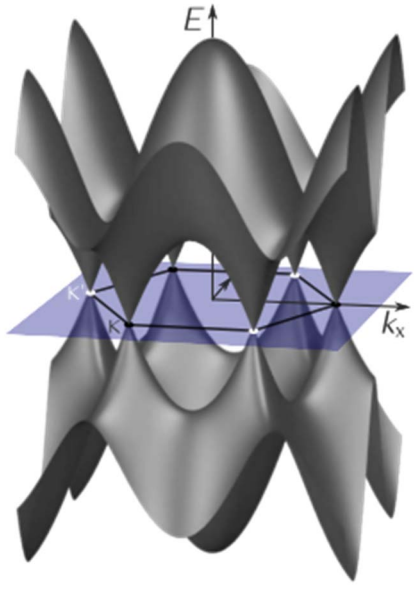


**Figure 2**. Electronic band structure of graphene. Reprinted from [23] using CC BY-SA 4.0 license.

The Fermi level of graphene is situated at Dirac points, where π band meets π* band; those points are situated at the corners of the graphene Brillouin zone. In total, as seen in Figure 2, there are 6 points like that, and they are grouped in two non-equivalent sets labeled K and K', consisting of three points each [24]. The Dirac points are thus a transition between graphene's valence and conduction band [25]. In the absence of an external electric field, the valence band of graphene is filled and the conduction band is empty, so graphene acts as a zero-gap semiconductor with low conductivity [24]. Graphene behavior can be altered by either an applied electrical field or doping, transforming it into either an n-type or p-type material, with electrons or holes as the main charge carriers, respectively [26].

In pristine graphene, the charge carriers are scarce, and they can travel long distances without colliding with each other. They behave as massless fermions, reaching high Fermi velocities of approximately $10^6$ m/s [18]. It is also noteworthy

that even in the case of the pristine graphene on a substrate under ambient conditions these charge carriers exhibit extremely high mobility, surpassing 15000 $cm^2 \cdot V^{-1} \cdot s^{-1}$ [27]. Electron waves propagate within a single layer of graphene and are more accessible to scanning methods compared to bulk materials. This also makes electronic properties highly sensitive to dopants adsorbed on the surface of graphene, making it an ideal material for gas sensor applications. On the other hand, intentional or inadvertent doping of graphene has the potential to significantly increase electron scattering on defects, thereby limiting charge carrier mobility. All this makes graphene highly sensitive toward even minor changes on its surface and allows the production of graphene devices with controlled electronic properties.

### 2.1.3 Production of graphene

Graphene is one of the carbon allotropes, a real one-atom-thick material consisting of a single atomic plane of graphite. After the initial reports from Geim and Novoselov [1, 27], graphene became a heavily researched material in multiple fields (electronics, sensors, solar cells). At first, micromechanical cleavage was used to produce graphene sheets, resulting in microcrystals with about 10 μm in size [1, 28]. In the following years, several other methods were developed to produce larger sheets of graphene materials, for instance the CVD of graphene on metals and the epitaxial growth on SiC by thermal decomposition [29].

The micromechanical cleavage method uses an adhesive tape to separate layers of highly oriented pyrolytic graphite. After multiple repetitions, this technique allows for obtaining an few-layer graphene (FLG) or single-layer graphene (SLG). Graphene produced by this method is of high quality since it is usually a single crystal and the contamination level of graphene is low. While this procedure is cheap, it is not a reliable way for the production of graphene flakes with certain dimensions repeatedly and is not applicable in terms of mass production. Micromechanical cleavage has widely been used to produce high-quality graphene for studying its physical and electrical properties in the lab [30].

CVD allows growing high-quality monolayer graphene on large metal foils (1 $m^2$), outperforming other growth techniques [31, 32]. Carbon-containing gas like methane is directed through a chamber with a heated foil, and, as a result of a chemical reaction carbon atoms uniformly cover a metal sheet producing SLG or FLG. Metallic foil is etched away as a next step and graphene is transferred onto a desired substrate. Graphene production by CVD method has been widely implemented and improved in the last decade. The end product can be controlled by a multitude of parameters like temperature, pressure, precursors, substrate material, gas flow and others. CVD grown graphene is not a single crystallite, but consists of grains of 1–20 μm in size. The grain boundaries might have a significant effect on graphene electrical characteristics [33]. Also, small-scale bilayer graphene formations are usually seen during scanning electron microscopy (SEM) analysis of CVD graphene. This, plus contamination from the graphene sheet transfer process and species adsorbed from the environment ($H_2O$, organic

residue) still requires improvements for CVD method, but at its current stage it is a reliable way of producing large-scale graphene sheets for research purposes.

Epitaxial graphene is grown from a SiC single crystal when the temperature of the substrate is high enough – a thin layer of graphene grows on top of the substrate when Si atoms are evaporated [34]. Due to the electronic coupling of graphene and SiC substrate, the epitaxial graphene is usually n-type [25]. This method is scalable and also does not require a transfer procedure, since graphene-based electronic devices can be produced directly on top of SiC. On the other hand, the charge transfer between graphene and substrate leads to a decline in the electrical properties of graphene. Moreover, the growth of epitaxial graphene is not cost-efficient when compared to the CVD method, as SiC substrates are more expensive than metal sheets used in CVD, and ultra-high vacuum and high temperatures are used during the process.

Reduced graphene oxide (rGO) is another material that is derived from graphene by chemical reduction of dispersed layers of oxidized graphite. rGO production is usually cheaper and allows to make larger quantities of material, but at the cost of its properties (damaged lattice structure, lower electronic conductivity) [35].

## 2.2 Gas sensors

Chemiresistive gas sensors based on semiconductor metal oxides (SMOX) are commonly used in the industrial sector for air monitoring. The operational principle of SMOX-based gas sensor relies on the interaction between the target gas and the surface of SMOX or the oxygen species adsorbed on its surface [36, 37]. Following the exposure to the target gas, sensor's electrical parameters, such as conductivity, change. The concentration of the target gas can be estimated by analyzing this change [37]. Sensor's response is caused by the charge transfer between adsorbed molecules and the sensor; molecules can act either as electron donors or acceptors [38]. However, SMOX sensors have certain drawbacks: they typically operate at elevated temperatures (200 – 400 °C), have relatively large signal drift and exhibit poor selectivity [39]. Moreover, the high power consumption hinders the application of SMOX-based gas sensors in handheld devices and usage for detection of flammable gases [37]. Elevated temperatures could be applied for graphene as well, but annealing it might lead to structural deformation and degradation of its electrical properties [40]. Therefore, visible and UV light illumination have been successfully implemented to enhance the performance of decorated graphene sensors [12, 41].

### 2.2.1 Key characteristics

Gas sensors are crucial devices designed for the detection of gases and the measurements of their concentration, which is achieved by converting the chemical reaction between the gas and the sensing material into a useful signal. Sensitivity,

selectivity, stability, repeatability and limit of detection (LOD) are some of the key parameters to evaluate the performance of a gas sensor.

Sensitivity is commonly represented as a change in sensor signal under the influence of the measured analyte compared to the signal in a reference environment, divided by the change in the analyte concentration. At times, sensors need to detect concentrations as low as parts per billion (ppb). Structure and porosity of the sensing surface, dopants, and operating temperature of the sensor are among the factors that influence the sensitivity of a sensor [42].

Selectivity represents the ability of the sensor to distinguish between different gases, ensuring that interfering gases do not significantly influence the response to the target gas during measurement. Selectivity can be achieved by modifying sensing material with specific catalysts to enhance the reaction with the individual target gas. Gas sensors are expected to perform their function in complex environments with multiple gases present; thus, achieving at least partial selectivity for a sensor is a high priority, leading to the acquisition of reliable data.

Stability is indicative of a gas sensor's long-term performance, reflecting its ability to collect reliable data under changing working conditions for a prolonged period. If the signal of a gas sensor fluctuates too much, especially with gas composition staying predominantly constant, it compromises the collected data.

Repeatability demonstrates consistency of obtained experimental data across experiments conducted under identical environmental conditions. Sensors need to recover from the contact with the target gas, as well as remain stable and operational under specified measurement conditions, to provide reliable data.

The LOD reflects the minimum concentration of the analyte that a gas sensor is capable of detecting under specified conditions. This parameter is also directly connected to the signal-to-noise ratio, a relation between the signal to the background noise.

Response and recovery times are temporal parameters related to the speed of reaction of the gas sensor to the analyte or its subsequent return to the baseline signal.

### 2.2.2 Graphene as a gas sensor

This study is an investigation of the gas sensing capabilities of pristine and PLD-modified graphene. Certain properties of graphene discussed in the previous sections make it an ideal candidate for gas sensor applications. Being a two-dimensional material, graphene's surface is fully exposed to the environment; graphene also has a low Johnson and 1/f noise, which has enabled detection of a single gas molecule adsorption on pristine graphene in highly controlled conditions in vacuum in 2007 [28]. The same research also featured graphene responses to 1 ppm concentrations of $NO_2$, $NH_3$, $H_2O$ and CO, with signal changes within the 1–5% range. Graphene's charge carriers are affected by adsorbates, with oxidizing gases such as $NO_2$ taking electrons away from the graphene thus promoting hole conductivity, while reducing gases like $NH_3$ introduce additional electrons into the system [43, 44]. Gas sensing relies on gas adsorption to the

surface, but the process is more complicated due to multiple competing processes happening simultaneously. Besides the target gas molecules adsorbing on the sensing surface, some of the adsorption sites are being filled by the other gas molecules coming from the surrounding atmosphere, and desorption of the gases is occurring. A 2010 investigation reported a 9% response to 100 ppm $NO_2$ using mechanically exfoliated FLG [45]. The paper reported that the $NO_2$ adsorption rate onto the pristine graphene surface was faster than the desorption rate, and the sensor had a slow recovery time; acceleration of signal recovery was suggested via the heating of the sensor or illumination of its surface by the UV lamp. In another research, a CVD graphene sensor showed analogous behavior when subjected to $NH_3$, with authors specifying its optimal operating temperature being in the 150–200 °C range [31].

It is noteworthy that pristine graphene is inadvertently doped by gas molecules present in the ambient air ($O_2$, VOC, water vapor [46]), as well as by residue chemicals left over from manufacturing and transfer processes. These impurities on the surface can either enhance or suppress graphene's sensitivity to specific compounds and getting rid of them requires meticulous sample preparation and annealing at high vacuum conditions, among other measures. For example, a structured water layer that can form atop of graphene was found to be strongly adsorbed to the surface even above 100 °C, the boiling point of water [47]. The authors noted that temperatures as high as 300 °C were necessary for its complete removal. Physisorbed $O_2$ molecules were successfully removed from the CVD graphene surface through thermal annealing at 413 K [48]. It is also worth mentioning that the changes in the relative humidity level in the ambient air influence the charge carrier concentration in the sensing layer [49].

One of the common elements of ambient air, $O_2$, has been documented as a p-type dopant when chemisorbed to CVD graphene [33, 50]. Graphene's behavior as either the n- or p-type material is contingent upon the nature of the adsorbates on its surface, and control over surface composition enables tuning of graphene carrier concentration [25]. Controlled functionalization of graphene should be considered for improving its sensing properties [46]. Functionalization of graphene with metals, metal oxides and other materials has demonstrated the capacity to achieve heightened responses to gases such as $NO_2$ and $NH_3$ when compared to pristine graphene [51–53]. Substantial research efforts have been dedicated to finding optimal materials and techniques for graphene functionalization [29, 54, 55]; researchers have been trying out covalent and non-covalent approaches, implementing decoration with both organic and inorganic molecules [6, 10, 56]. Several techniques have been employed for graphene functionalization, including hydrogenation, fluorination, treatment with ammonia or nitrogen plasma for covalent modification. For less destructive material manipulation, non-covalent functionalization via weak van der Waals interactions between graphene surface and attached molecules could be used [57].

Additionally, the correct choice of a dopant increases the selectivity, as specific dopants can be chosen to bind certain gas molecules while exhibiting weaker interactions with others. Platinum [58], palladium [59], gold [60], titanium

oxide [61] and many other materials have been reported to be used as functionalization components in graphene-based gas sensors [62]. Single-layer graphene functionalized by photoactive $TiO_2$ achieved great oxygen sensitivity in a wide concentration range (5–100%) [63]. Enhanced $NO_2$ sensing has also been achieved via the decoration of graphene surface with monodisperse polystyrene beads [64]. Gas responses to 500 parts per trillion (ppt) $NO_2$ were achieved with S-doped CVD graphene sensors on a micro-hotplatform [65]. It is worth mentioning that the increased gas sensitivity and selectivity are often achieved at a compromise of making the electrical properties of graphene worse since the crystal lattice of graphene is damaged. This is evidenced by numerous Raman measurements where the intensity of the 2D line is lower than that of pristine samples, and by the diminished conductivity of the samples after functionalization [66]. This tradeoff is necessary for obtaining gas sensors with enhanced response and recovery times and improved selectivity. Finding a balance between disrupting the graphene lattice and introduction of the dopants is crucial, as excessive damage can lead to the destruction of the graphene structure, rendering samples unresponsive.

PLD is a flexible method for surface decoration. A wide range of materials can serve as ablation targets: in addition to common oxides, nitrides, and metals, high melting point metals such as tungsten can also be used [67]. Laser parameters such as pulse duration, fluence, and wavelength can be manipulated. Moreover, factors like the distance between the ablation target and substrate, working temperature, and the background gas in the chamber are adjustable [68]. Using the pressure of inert gases in a PLD chamber as a tuning tool, it becomes possible to regulate the velocity of plasma ions. This permits to control the extent to which the graphene structure would be damaged during PLD.

The kinetic energies of plasma particles within the range of 5 and 20 eV are sufficient to break C-C bonds in graphene, and these particles could replace C atoms within the lattice. Additionally, laser properties such as wavelength, pulse duration, and laser fluence, can all be tuned to improve the sample preparation process. Hybrid materials, obtained as a result of the partial disruption of graphene lattice and the incorporation of new adsorption/catalytic centers, exhibit significantly improved gas sensitivity. For example, $ZrO_2$ exhibits promising catalytic and optical properties, making it an excellent candidate for activating graphene gas sensors. Previous studies have shown that $ZrO_2$ enhances the photocatalytic activity of graphene [69]. The addition of noble metals, such as Ag or Au, has also been demonstrated to improve the gas sensitivity of graphene-based sensors [70–72]. A single-layer CVD graphene doped with Ag nanoparticles (via treatment with $AgNO_3$ and $Fe(NO_3)_3$ solution) had improved sensitivity to $H_2S$, with authors citing the generation of $H_2S$ adsorption and dissociation sites on graphene surface after functionalization [73]. $TiO_2$, a semiconducting oxide, acts as an n-type semiconductor [74] with a large band gap energy of 3.0 eV for rutile and 3.2 eV for anatase [75, 76]. $TiO_2$ is extensively researched for implementation in gas sensors, solar cells, and optoelectronic devices [77]. The synergistic effect of $TiO_2$ and graphene has shown great potential for $NO_2$ gas sensors [63, 72]. It was

also utilized in combination with reduced graphene oxide for improved $NH_3$ detection in the range of 5 to 50 ppm [78]. $V_2O_5$ has been utilized in $NO_x$ selective catalytic reduction using $NH_3$ and is a promising candidate for $NH_3$ detection when deposited on top of graphene [79].

Exposing the graphene surface to light has the potential to remarkably enhance the performance of gas sensors. Light achieves multiple goals: surface cleaning before the experiments, photoexcitation of charge carriers, and accelerated signal recovery to the baseline between and after measurements [80]. UV light illumination was used successfully to move Dirac point of graphene to 0 gate voltage from initial non-zero state [81]. A characteristic trait, known as negative persistent photo-conductance, was commonly observed when graphene was exposed to UV light. A decrease in conductance under UV light is attributed to de-doping of the surface [82]. Graphene typically exhibits p-type conductivity in the air due to the adsorption of $O_2$ and $H_2O$, which take electrons from graphene and promote hole conductivity [82]. UV light has the potential to partially reverse this effect [9]. UV light has been used to improve the recovery times of single-wall nanotubes signal after contact with target gases by means of photodesorption [83]. Further research has demonstrated that continuous UV illumination during measurement can lead to improved gas responses [84]. Since then, research on UV light influence on sensor properties of a wide variety of materials has been conducted [85–88]. It was shown that de-doping occurs under UV light – a negative shift of Dirac point was observed from 70 V (indicating p-type graphene) to 5 V (much closer to the intrinsic graphene) during a 60-minute exposure of graphene to UV light [89].

# 3. EXPERIMENTAL GOALS AND THE STRUCTURE OF THE STUDY

The main goal of the research presented in this thesis was to investigate how UV light irradiation affects the performance of the gas sensors based on single-layer CVD graphene in relation to the detection of oxidizing gases ($O_2$ and $NO_2$). In particular, the aim was to study and improve the gas sensing properties of pristine and PLD-modified graphene sensors via optimization of irradiation parameters and identification of suitable materials and fabrication conditions (amount of transferred material, deposition parameters) for PLD functionalization.

In the first part of the work, pristine CVD graphene was illuminated by UV light and the effect of irradiation on oxygen sensitivity was studied. It was also important to investigate the influence of irradiation on the electrical characteristics of graphene. It was expected that UV light should activate the sensing properties of the graphene layer by freeing the adsorption sites on its surface from the environmental adsorbates.

In the second part, graphene functionalized with metallic Ag and dielectric oxide $ZrO_2$ was studied. It was expected that the creation of new adsorption sites with PLD will improve the gas sensitivity of graphene-based gas sensors. A series of depositions with each of the materials were performed to investigate the effect of PLD on graphene's structure (damage to the lattice, surface coverage) and gas sensing properties to $NO_2$ gas.

In the third part of the work, results obtained with graphene-$TiO_2$ heterostructure are discussed, where the functionalization of graphene by a nanolayer of oxide material is combined with UV light irradiation. The beneficial synergy between light and photocatalytic $TiO_2$ was anticipated to play an important role in the gas sensing properties, and the UV light (wavelength of 365 nm) effect was compared to visible light (436 and 546 nm). Cross-sensitivity tests with other major polluting gases like $NH_3$, CO and $SO_2$ were performed and compared to the results obtained during $NO_2$ experiments.

# 4. EXPERIMENTAL DETAILS

## 4.1 Sensor preparation

To investigate the gas sensing characteristics of pristine and modified graphene, a series of graphene sheets were synthesized using the CVD method. The process was conducted in a custom-built hot wall quartz tube CVD reactor. A gas mixture of 10% $CH_4$ in Ar (99.999%) was passed through a chamber containing polycrystalline copper foil that was previously annealed at 950–1000 °C in $Ar/H_2$ (both 99.999%) for 25–40 min. Graphene layer was grown on the Cu foil, and subsequently, the graphene side of the sample was covered with PMMA using spin coating. The PMMA/graphene/Cu sample was then floated on a 0.1M aqueous $FeCl_3$ solution to dissolve Cu. The films were then transferred to deionized water to eliminate residual copper etchant. Graphene sheets were transferred onto $10\times10$ $mm^2$ $Si/SiO_2$ substrates with Ti/Au electrodes formed by electron beam deposition through a shadow mask. In the final step of sample preparation, PMMA layer was dissolved in dichloromethane. For selected samples, the back side of the Si plate was cleaned with HF, and a Ti/Au layer was grown there to form a back-gate electrode. A photograph of the gas sensing device is presented in Figure 3, where the graphene sheet, partially covering metallic electrodes, is visible on top of the substrate due to the reflective properties of graphene.

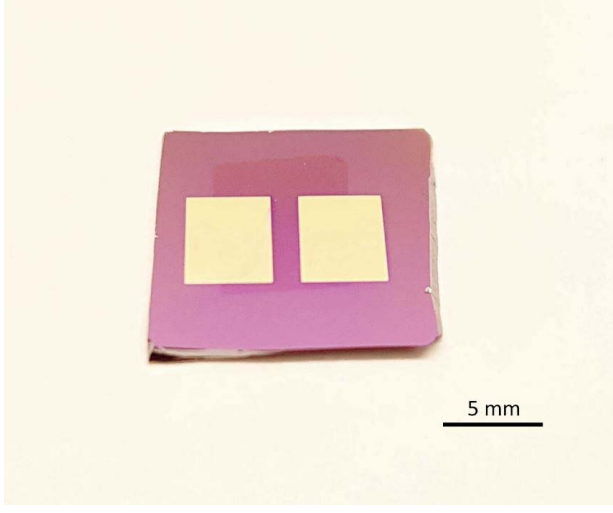


**Figure 3.** Photograph of a graphene-based gas sensor device. Graphene sheet can be seen on top of $Si/SiO_2$ substrate with Ti/Au electrodes because of its reflection properties. Gap between electrodes ($1 \times 4$ $mm^2$) was targeted during PLD process for oxide/metal deposition. Adapted from **Paper III** under CC-BY 4.0 license.

Following the analysis of pristine graphene using Raman spectroscopy and other methods described later in this section, PLD was used to functionalize some of the graphene samples by depositing metal or metal oxide on their surfaces. For the procedure, graphene sensor substrate was placed into the PLD chamber, which was then evacuated to $10^{-6}$ mbar. Then substrate was heated *in-situ* at 150 °C for 90 min to clean the surface from potential contaminants remaining after graphene sensor manufacturing phase. Subsequently, the sample was cooled down to room temperature, and the deposition was performed. Oxides ($ZrO_2$, $TiO_2$) were ablated in the presence of $5 \times 10^{-2}$ mbar of oxygen, while Ag was deposited with $5 \times 10^{-2}$ mbar of nitrogen used as a background. The target materials were pressed into pellets and baked at 550 °C in air for 5 h before deposition. A KrF excimer laser with a wavelength of 248 nm and a pulse width of 25 ns was utilized for deposition. During the ablation, the laser pulse energy density was set to 2.5–5.0 J/cm$^2$.

After functionalization, gas sensors underwent analysis by Raman spectroscopy, and gas sensing properties were measured before a new cycle of PLD was performed with the same sample to determine the optimal functionalization level for each material. Raman spectroscopy is a versatile non-destructive method for examining graphene samples, offering insights into the number of graphene layers and their orientation, the degree of lattice disorder, and the presence of defects. After completing all planned measurements, SEM pictures of the samples were taken to visualize the structure of the deposited material on top of graphene. SEM is a technique used to gain information about a material's topography by scanning the surface with an electron beam. Excited atoms emit secondary electrons, and the intensity of the measured signal is interpreted into information about sample's surface.

## 4.2 Experimental setup

Gas sensitivity measurements of graphene samples were conducted in a stainless steel sample chamber with a total volume of approximately 7 cm$^3$. Schematic representation of the measurement setup can be seen in Figure 4. The gas system was equipped with a series of mass flow controllers (Brooks Instrument, model SLA5820) to precisely control the composition of the gas mixture directed into the test chamber. The total gas flow through the test chamber was maintained at a constant 200 sccm, and the final gas composition reaching the test chamber was regulated by separately adjusting the gas flow rates of each used gas through the mass flow controllers. A synthetic air mixture composed of 79% $N_2$ and 21% $O_2$ was used as the main carrier gas during the gas sensitivity experiments to emulate ambient air conditions. To control the humidity level in the test chamber, a water bubbler was connected to the gas system, allowing a portion of $N_2$ to pass through it, thereby saturating it with water vapor. The gases used in the measurements, $N_2$, $O_2$, $NO_2/N_2$, and $NH_3/N_2$, were all of high purity (99.999%). The system operated under normal atmospheric pressure, with the gas flowing through the measurement chamber during the experiments.

The entire operation was controlled by custom-designed software developed using LabView. Electrical measurements were conducted using a source meter Keithley 2400 (Keithley Instruments). After testing several samples with different voltage values, it was determined to maintain the applied voltage between two electrodes on top of graphene at 100 mV. Experiments with higher and lower voltages did not directly impact the gas responses of the graphene sensor samples. A back-gate electrode was created on the back side of the Si plate before graphene transfer, to enable the measurements of field effect transistor characteristics for selected sensors. HF was used to clean back of the Si plate before the evaporation of the Ti/Au layer to ensure a good contact. A second source meter, Keithley 2450, was used to apply voltage between one of the top electrodes and the back-gate.

During measurements of gas responses under UV light excitation, a Xe-Hg high-pressure lamp (L2422, Hamamatsu Photonics) was utilized. The fitting wavelength (365, 436, or 546 nm) was selected using a narrow-band interference filter (Andover) placed between the light source and a measurement chamber, with a water-filled filter used to cut off infrared light from the light source. The measurement chamber lid had a transparent window, which allowed to guide the light onto the graphene area between the two electrodes. In all experiments, the irradiance of light on the sample ranged between 10–20 mW/cm$^2$. Tests involving turning room lights on and off did not show any effect on the measured electrical signal.

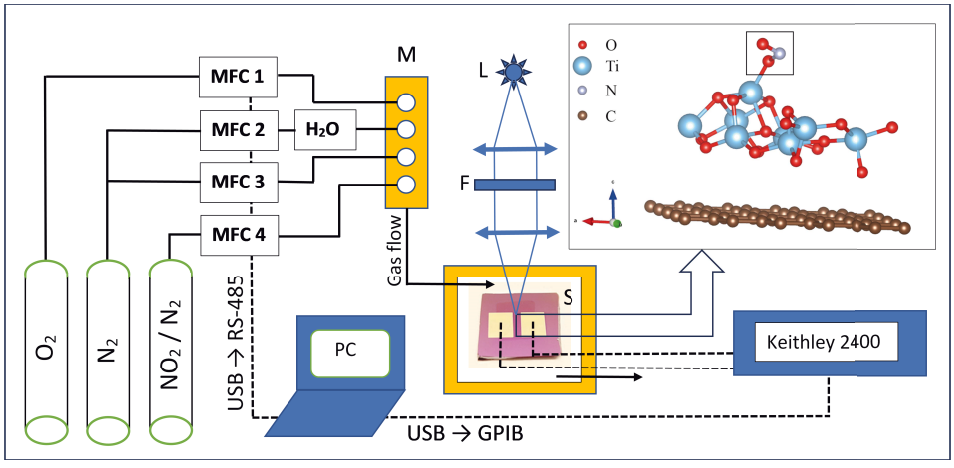


**Figure 4**. Measurement set-up scheme. Schematic representation of graphene and $TiO_2$ with adsorbed $NO_2$ is shown on inset. Reprinted from **Paper III** under CC-BY 4.0 license.

## 4.3 Characterization techniques

After the sample preparation was finished, several characterization techniques were employed to gain additional information about the quality of graphene and the impact of PLD on sample characteristics. Raman spectroscopy (Renishaw inVia micro-Raman spectrometer, 514.5nm excitation wavelength, incident power 1 mW) was used to analyze the quality of graphene, including the presence of multilayer graphene regions and defects. FEI Helios NanoLab 600 electron microscope was used to capture images of the sample surface. SEM images were acquired only after the final PLD phase to prevent the influence of the electron beam on graphene, thereby avoiding potential structural damage to the graphene lattice and subsequent impact on the gas sensitivity of the samples. X-ray fluorescence (XRF; Rigaku ZSX-400) and ellipsometry (GES-5E) methods were applied to PLD-modified samples to assess the amount and thickness of material transferred onto graphene during deposition. The oxidation state of metals was determined using X-ray photoelectron spectroscopy (XPS; Scienta SES-100). A polychromatic twin-anode X-ray tube (Thermo, XR3E2) with Mg $K_\alpha$ (1253.6 eV) 300 W irradiation was used as an excitation source.

# 5. RESULTS

## 5.1 Pristine graphene

Following the fabrication of graphene sheets and its transfer onto the $Si/SiO_2$ substrate as described in the previous section, the characterization of pristine graphene using optical microscopy, Raman spectroscopy and SEM, was performed. Samples exhibiting good surface morphology with a minimal number of defects were selected for gas sensing measurements and as a base for functionalization with PLD.

The typical Raman spectrum of the pristine graphene used in this study, captured between the metallic electrodes, is depicted in Figure 5a. It fits a Raman spectrum of a single-layer CVD graphene with a low number of defects. Graphene-related G- and 2D-band peaks were generally located at 1583–1590 $cm^{-1}$ and 2680–2690 $cm^{-1}$, with full widths at half maximums ranging from 14–20 $cm^{-1}$ and 30–40 $cm^{-1}$, respectively, and the ratio of the band intensities being close to 1:3. The G-band corresponds to the carbon-carbon in-plane vibrational mode, while the 2D-band, an overtone of the defect-related D-band, is connected with the breathing mode of aromatic rings. The 2D-band exhibited a single Lorentzian shape, characteristic to single-layer graphene. The D-band, revealing the presence of crystalline defects, was infrequently observed at 1350 $cm^{-1}$, mainly when scanning close to the Au electrodes or the edges of graphene. Raman two-dimensional mapping indicated that the area ratio between 2D- and G-bands commonly was in the range of 5–6. Based on all the information gathered from the Raman spectra, it was concluded that pristine graphene was predominantly single-layered and defect-free.

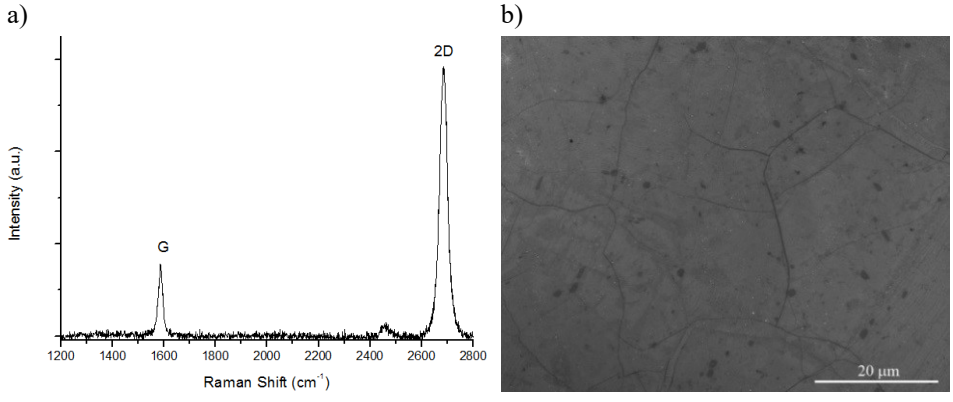


**Figure 5**. a) Raman spectrum and b) SEM image of pristine graphene on $Si/SiO_2$, both taken between the electrodes (graphene on $Si/SiO_2$). Reproduced from **Paper I** with the permission of AIP Publishing.

Figure 5b presents a typical SEM image of the CVD-grown pristine graphene. The image, taken between two metallic electrodes, reveals the nonuniformity of the graphene layer and shows grain boundaries; the size of crystallites was between 1 and 10 µm. The polycrystalline structure of CVD graphene is largely regulated by the topography of the metal foil used during the synthesis phase [90]. Additionally, some wrinkles in the graphene sheet might be introduced during its transfer from the Cu-foil to the $Si/SiO_2$ substrate. Darker areas on the graphene can be attributed to small multilayer formations.

Both Raman spectroscopy and SEM have confirmed the overall nature of CVD graphene as a mostly single-layer polycrystalline material with a minimal number of lattice defects. Raman and SEM images of functionalized graphene are discussed in the next chapter of this work, both confirming the introduction of defects into the graphene structure during the PLD process. Following graphene functionalization, the D-band becomes more prominent in the Raman spectra, and newly grown nanostructures are observable in SEM images.

Field effect transistor characteristics were measured on selected pristine graphene samples. Through the tuning of the back-gate voltage, the Fermi energy can be manipulated, allowing for the alteration of the type of charge carriers from holes to electrons and vice versa [91, 92]. The dependence of drain-to-source current, $I_{ds}$, on the back-gate voltage, $U_G$, was measured both without and under UV illumination in synthetic air. Figure 6 illustrates a single sweep from 30 V to –30 V and back.

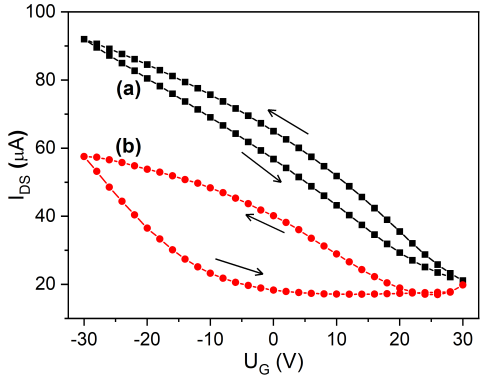


**Figure 6**. Transfer characteristics curves of graphene in dry synthetic air (a) before and (b) under illumination. UV light (365 nm, intensity 20 $mW/cm^2$) was used during this experiment. $U_G$ scan rate was 0.067 V/s. Reproduced from **Paper I** with the permission of AIP Publishing.

In synthetic air, it is evident from the data that the graphene probes are p-type, as the Dirac point is shifted to ~30 V, rather than being located at 0 V [93]. This shift is likely attributed to the presence of oxygen and water molecules adsorbed on the graphene surface from the ambient air [81, 94]. Additionally, the substrate inadvertently influences the properties of graphene, contributing to the shift in the charge neutrality point [95]. The electrical current level is lower in UV-illuminated measurement due to the light cleaning the surface of adsorbed molecules,

which is in accordance with findings in the literature and our own experiments [12, 89, 96]. Figure 6 also illustrates that the Dirac point under UV light is shifted from beyond 30 V closer to the 0–25 V range since $I_{ds}$ started to grow at $U_G > 25$ V. This indicates the ambipolar transport properties of the sample at $U_G = 25$ V under UV light, with both electrons and holes present with equal density [94, 97]. For the pristine graphene used in this work, hole mobility in the range of 1000–4000 $cm^2/Vs$ was determined.

Both curves exhibit hysteresis, with measured values on the way from 30 V to –30 V and on the way back not being identical. Hysteresis is also more prolific under UV light. The phenomenon may be caused by interfacial or surface charge traps, where hole charge carrier transfer between graphene and traps occurs during the measurement. Contrary to the expectation of smaller hysteresis under UV light, which should aid with surface de-doping, the opposite is observed in Figure 6b. Besides clearing the surface from adsorbed oxygen/water, light appears to be responsible for the photo-activation of traps, resulting in an even more significant offset compared to measurements without UV light.

A typical gas response of pristine graphene to $NO_2$ and $NH_3$ is depicted in Figure 7. In this work, the sensor response is presented as a relative change in electrical conductance, G (or electric current, I):

$$S = \frac{G - G_0}{G_0} \tag{1}$$

where $G_0$ is the conductance in synthetic air at room temperature.

For both 4 ppm $NO_2$ and 30 ppm $NH_3$, it is evident that at room temperature without UV excitation, responses of unmodified samples are practically negligible (less than 1%). The situation significantly changes when 365 nm UV light is directed at the graphene between two metallic electrodes – responses to both gases improve drastically, registering a 15% relative signal change ($\Delta G/G_0$) within 10 minutes. In both cases, a p-type response was observed, with conductance increasing upon contact with $NO_2$ and decreasing with $NH_3$.

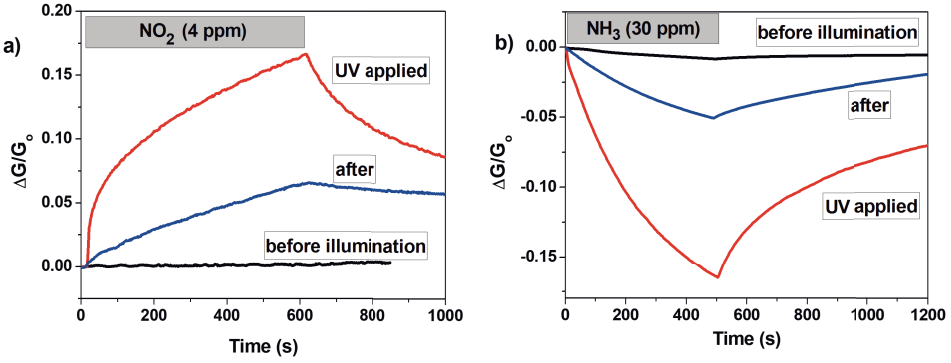


**Figure 7**. Response of pristine graphene to (a) 4 ppm $NO_2$ and (b) 30 ppm $NH_3$ measured with and without exposure to the UV light.

As mentioned in the preceding section, $NO_2$ and $NH_3$ behave differently while interacting with pristine graphene gas sensors – the former acts as an electron acceptor (hole donor), while the latter serves as an electron donor [44]. This explains the signal change in opposite directions – $NO_2$ promotes graphene's hole conductivity even further, causing an increase in signal, while $NH_3$ causes a decrease in conductivity [93]. It is noteworthy that relatively high concentrations of $NO_2$ and $NH_3$ were used for the initial experiments with pristine graphene, with plans to reduce concentrations after graphene functionalization.

The enhanced gas response persisted even after turning off the UV light source – responses to $NO_2$ and $NH_3$ were smaller, and signal recovery was also affected, but overall sensor performance remained superior to that of pristine graphene without UV. This effect typically disappeared after 24 hours but was reproducible after subsequent UV light applications.

Detection of polluting gases using a chemical sensor inevitably occurs in ambient air with the presence of oxygen and water vapors. Moisture interaction with the surface of graphene is described as physisorption since the sensor response is reversible and sensitivity decreases with the increase in temperature [98]. Therefore, some potential adsorption sites are occupied by these "background pollutants" (surface coverage factor = 1). When $NO_2$ or $NH_3$ molecules come into contact with the graphene surface, they are unable to connect with the surface, resulting in minimal impact on the electrical properties of graphene. UV light, however, activates the surface, cleaning it from loosely attached molecules and creating adsorption sites for $NO_2$ and $NH_3$ (coverage factor < 1). When the UV source is removed, the equilibrium shifts again. With no additional target gas molecules appearing, adsorption sites are gradually filled with oxygen and water vapor molecules over time.

The impact of oxygen removal from the synthetic air mixture was tested during the experiment depicted in Figure 8. The measurement was conducted with and without UV light at two different relative humidity levels, RH = 0% and RH = 50%. Oxygen was removed from the synthetic air mixture for 10 minutes at all three stages of the experiment – before, during and after UV light application to the graphene surface.

Before the start of the experiment, the samples were exposed to the synthetic air mixture for an extended period of time. Subsequently, oxygen was removed from the mixture, and only $N_2$ was introduced into the measurement chamber. The transition from synthetic air to pure $N_2$ and back to synthetic air was nearly unnoticeable without the influence of UV light, as the measured electrical signal change was below 1%. This indicates that, without external energy applied, $O_2$ molecules attached to the graphene do not desorb from the sensor surface when oxygen flow into the chamber stops.

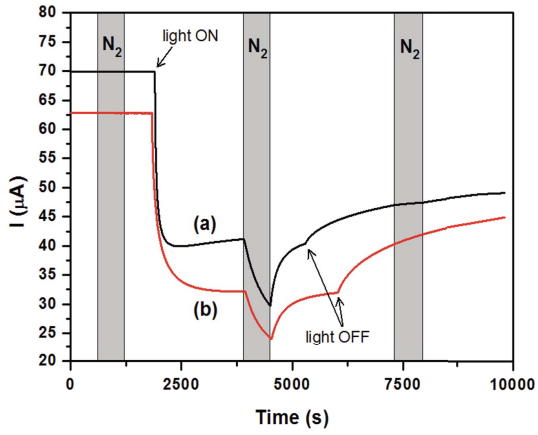


**Figure 8**. Graphene sensor's current in dark and under illumination in synthetic air (white areas) and pure nitrogen (grey) at (a) RH0% and (b) RH50%. The wavelength of light was 365 nm, and the intensity was 20 mW/cm$^2$. Reproduced from **Paper I** with the permission of AIP Publishing.

In the next phase, UV light was applied to the graphene surface. After the electrical signal stabilized, the same procedure of $O_2$ removal from the gas mixture was repeated. The impact under UV is evident, indicating that UV light can transfer energy to facilitate the desorption of molecules from the sample surface. When the flow of $O_2$ into the chamber stops, a signal decrease is registered. $O_2$ molecules desorb under UV light influence, returning electrons back into the system and thus decreasing the p-type conductivity characteristic of CVD-grown graphene on Si/$SiO_2$. Upon reintroduction of $O_2$ into the system, the signal climbs back almost to the initial level, confirming the reversibility of this process. The registered response within 10 minutes is greater than 25%.

After switching off the UV light, the electrical signal slowly returned to the initial levels. Without UV excitation, the removal of $O_2$ from the mixture had a negligible effect on the sample signal. It usually took from several hours to two days for a sample to revert to its initial state after the use of UV light, which is significantly longer compared to the rapid reaction and signal drop when UV light was turned on.

The effect of oxygen removal is relatively similar at both RH = 0% and RH = 50%. The amplitude of the response is higher during measurements in dry conditions because there is no competition for adsorption sites between water vapor and $O_2$. This leads to more oxygen molecules interacting with the graphene surface, directly influencing its electrical characteristics.

The measured electrical signal decreases significantly under UV light excitation, and recovery starts only after UV light removal. This behavior is consistent for all the graphene samples used in this research and is discussed in more detail in the next chapter. In Figure 8, a 50% decrease is registered under optical excitation, and the effect is even greater in the absence of $O_2$ at the start of the experiment, as seen in Figure 9.

The series of pristine graphene sensor responses to different oxygen concentrations in the $O_2/N_2$ mixture are shown in Figure 9. Initially, the sample was held in the chamber in pure nitrogen with a UV lamp turned off. Then, the light was switched on, and after 1,5 h of signal stabilization, mixtures with different $N_2/O_2$ ratios were introduced into the chamber, with a return to the pure $N_2$ in-between.

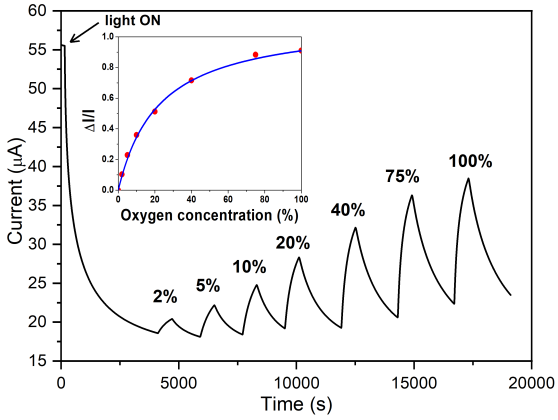


**Figure 9**. Pristine graphene sensor response to the different oxygen concentrations in $O_2/N_2$ mixture. Reproduced from **Paper I** with the permission of AIP Publishing.

Oxygen chemisorption $O_2 + e^- \leftrightarrows O_2^-$ leads to oxygen anion formation on the surface, with oxygen taking electrons from graphene [99]. The response dependence on oxygen concentration was successfully approximated by applying Langmuir's law:

$$\frac{\Delta I}{I} = \frac{cx}{1 + bx} \tag{2}$$

This law is suitable for a homogeneous material with clearly defined adsorption sites, describing the concentration dependence of the relative response reliably. Here, x represents the oxygen content in the gas, c is the sensitivity at low oxygen concentrations, and b is the affinity constant. The data from Figure 9 indicates that responses increased linearly at lower oxygen concentrations, but saturation started to occur with an increased $O_2$ percentage in the mixture.

## 5.2 Graphene functionalized with $ZrO_2$ and Ag

Surface cleaning through UV light exposure can sensitize graphene conductivity towards reactive gases such as $O_2$, $NO_2$ and $NH_3$, as demonstrated in the previous section. However, a more radical improvement in sensor behavior can be via the functionalization of graphene. The PLD method was found particularly well-suited for graphene modification due to its versatility in material choices. The deposition targets were selected with the catalytic (Ag) and photocatalytic ($ZrO_2$) activities in mind, involving redox reactions with the target gases ($NO_2$, $O_2$).

A series of PLD depositions were made on top of graphene supported by a $Si/SiO_2$ substrate. Raman measurements were performed between each PLD cycle to evaluate the changes in gas sensitivity of the sensor, and estimate the damage done to the graphene structure with each deposition. In the Raman spectrum of pristine graphene, the two main visible bands, G- and 2D-bands, were located at approximately 1586 $cm^{-1}$ and 2686 $cm^{-1}$, with full widths at half maximums of approximately 15 $cm^{-1}$ and 30 $cm^{-1}$, respectively. The Raman spectra also show that the defect-related D-peak at the 1350 $cm^{-1}$ region was almost absent in the pristine graphene (refer to Figure 10).

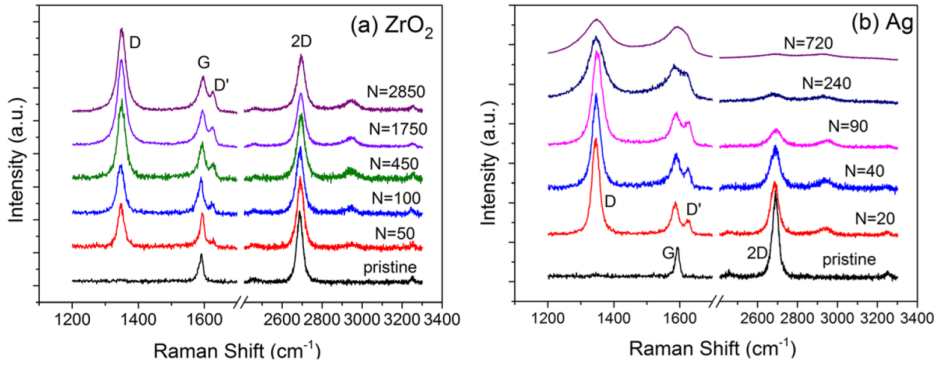


**Figure 10**. Raman shift of (a) $ZrO_2$- and (b) Ag-modified graphene. N signifies the number of used PLD laser impulses. Reproduced from **Paper II** with the permission of AIP Publishing.

During the PLD process, a total of 2850 laser pulses of $ZrO_2$ and 720 pulses of Ag were applied to the graphene. In the case of $ZrO_2$, the intensity of the D-peak increases with each new PLD cycle. D-peak also becomes noticeable in the case of Ag. Additionally, a D'-peak appears in both $ZrO_2$- and Ag-modified graphene Raman spectra at about 1625 $cm^{-1}$, further confirming the defectiveness of decorated graphene. The number of PLD pulses for each of the 5 steps can be found in Figure 10. The main difference in Raman spectra of graphene functionalized with metal oxide $ZrO_2$ and metallic Ag is the significant damage to graphene structure caused by subsequent Ag depositions. This is evident in Figure 10b, where, besides the rapid formation of intense D-peak, the broadening of the peaks occurs up until the last deposition with 720 pulses (D-peak broadening up to 120 $cm^{-1}$). In the case of $ZrO_2$, spectra change only slightly following the 450 PLD pulses deposition, with broadening of the D-band becoming saturated at 29 $cm^{-1}$.

SEM pictures of $ZrO_2$ and Ag might explain the reason behind this difference in Raman spectra (Figure 11). SEM measurement was only performed after the last PLD deposition and gas measurements in the series to avoid additional sample modification by the electron beam, which could've negatively affected gas sensitivity measurements.

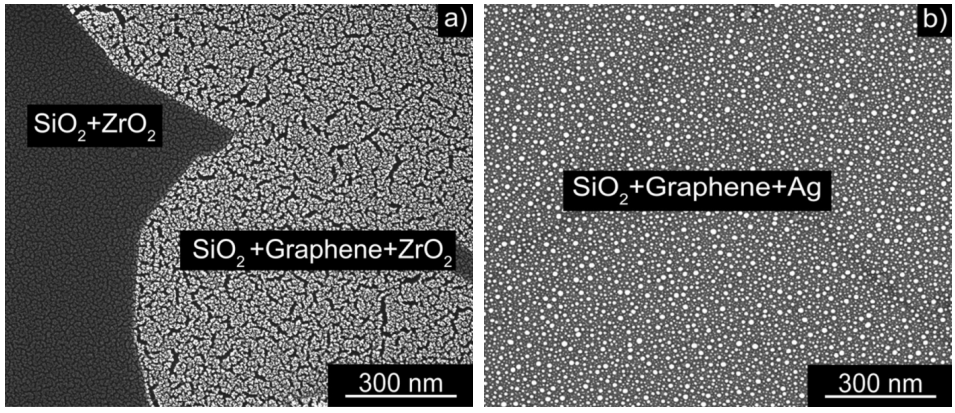


**Figure 11**. SEM image of (a) $ZrO_2$ and (b) Ag modified graphene. Reproduced from **Paper II** with the permission of AIP Publishing.

The surface of graphene is covered by a porous granular structure when $ZrO_2$ is deposited, while Ag does not cover the entire surface, concentrating into smaller clusters instead. The more serious deterioration of the graphene structure caused by Ag than by oxides might be explained as follows: after the first couple of PLD depositions, the graphene surface is covered by an oxide film that protects the underlying graphene from high-energy particles coming from the ablation target in following PLD cycles. In the case of metallic Ag that agglomerated into clusters, a higher percentage of the graphene structure is not protected by the metal deposited in previous cycles, and additional defects are introduced into the graphene. Data obtained by ellipsometry and XRF helps to confirm this statement – in the case of $ZrO_2$, pores and voids cover about 50% of the surface, while Ag covers only 10% of the graphene surface. Nominal thickness and percentage of pores of the deposited layers, $d_E$ and PP, obtained from ellipsometry data were 14 nm and 47% for $ZrO_2$ and 10 nm and 89% for Ag, respectively. The calculated thickness of materials without pores $d_1 = d_E \times (100 - PP)/100$ was approximately 6.6 nm for $ZrO_2$ and 1 nm for Ag.

In Figure 12, it is seen that the conductance of the samples measured in air decreases after each PLD cycle. For Ag and $ZrO_2$, this decrease followed the power law, with power indices –0.4 and –1.1, respectively. This is also in agreement with Raman spectra, where Ag had a more destructive effect on the sample, broadening Raman bands and causing 2D band disappearance.

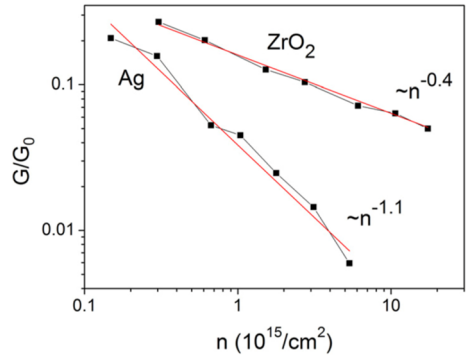


**Figure 12**. The dependence of the sensor's normalized conductance on the areal density of the deposited materials on graphene surface. Reproduced from **Paper II** with the permission of AIP Publishing.

The more prominent effect of Ag deposition on conductivity might also be explained by the work functions of the two materials. Given that graphene has a higher work function (4.7 eV) in contrast to Ag (4.3 eV), the doping by Ag leads to a decrease in the p-type conductivity of the sample. Conversely, $ZrO_2$ exhibits p-type conductivity at normal conditions, with a work function exceeding 5.35 eV. Consequently, doping from $ZrO_2$ will promote the p-type conductivity of graphene even further.

Figure 13 represents the responses of (a) $ZrO_2$- and (b) Ag-modified graphene to $NO_2$ gas. Four different $NO_2$ concentrations (40, 100, 300 and 1000 ppb) were used during the experiment. Measurement was performed with dry synthetic air as a carrier gas, at room temperature, in the absence of external illumination, and later under exposure to 365 nm light. The applied UV light intensity was 20 mW/cm$^2$. Analogous to pristine CVD-grown graphene, the interaction of $NO_2$ with functionalized graphene samples promoted p-type conductivity, causing an increase in signal.

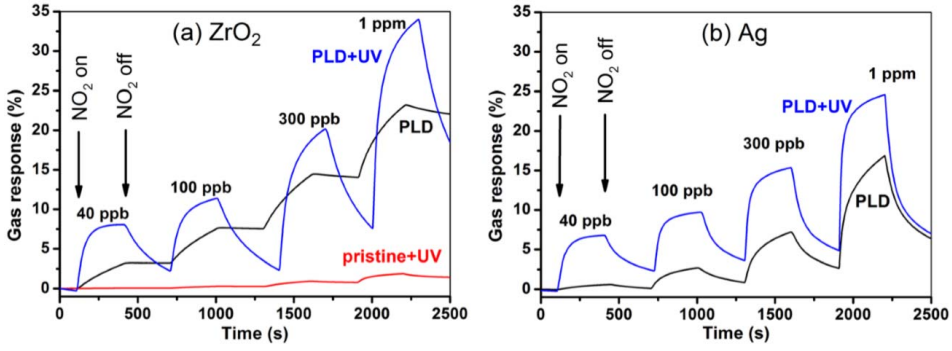


**Figure 13**. Responses of (a) $ZrO_2$ and (b) Ag modified graphene to $NO_2$ gas. Reproduced from **Paper II** with the permission of AIP Publishing.

The responses to $NO_2$ improved significantly after the functionalization of pristine graphene with either $ZrO_2$ or Ag. In Figure 7, the gas response of pristine graphene to 4 ppm $NO_2$ amounted to approximately 15% after 10 minutes; however, the functionalized graphene demonstrated a response of approximately 10% to a concentration 40 times lower, i.e., 100 ppb. The heightened gas responses can be attributed to an increased density of adsorption sites available for $NO_2$ interaction, coupled with a greater affinity of these sites toward the target gas. According to the first principle studies, the adsorption of $NO_2$ on regular graphene planes at room temperature is described as a weak interaction (adsorption energy $E_a < 0.07$ eV) [100]. However, in the case of defective or doped graphene, the adsorption becomes more pronounced, with adsorption energy ranging from 0.3 to 3 eV [11, 101].

The main difference between the oxide- and metal-doped samples during the experiments without UV light is the recovery rate after $NO_2$ flow into the chamber is stopped. The signal of Ag-modified graphene is capable of recovering to the initial level much faster than the $ZrO_2$ counterpart. Also, the response speed of the Ag-modified sample is faster both with and without UV light assistance.

The time-dependent signal changes of graphene samples were analyzed by fitting curves with single and double exponential functions. The curves have been divided into two phases: the response to the target gas and the subsequent recovery from it. Generally, a single exponential could be used to describe adsorption on homogeneous adsorption sites. However, the responses of most functionalized graphene samples were better approximated by double exponential functions. This suggests the occurrence of multiple processes with different kinetics simultaneously unfolding on the surface [79, 102]. Moreover, this type of kinetics may be regulated by the competition in adsorption between the target gas, $NO_2$, and other gas species such as $O_2$ and $H_2O$, known to adsorb on the graphene surface. The following equation was used for fitting:

$$G(t) = G_0 + A_1\left[1 - e^{\frac{-(t-t_0)}{t_1}}\right] + A_2\left[1 - e^{\frac{-(t-t_0)}{t_2}}\right] \quad (3)$$

In Equation (3), $G_0$ represents the conductance at the start of the experiment, and $G(t)$ is the conductance at time $t$; $t_0$ denotes the moment at which the gas mixture flowing into the chamber is changed. $A_1$ and $A_2$ represent amplitudes of conductance change, while times $t_1$ and $t_2$ are inverse first-order rate constants for the adsorption and desorption kinetics of gas molecules for functionalized graphene. For a single exponent fitting, only one set of parameters ($A_1$, $t_1$) from Equation (3) was used.

The gas sensor response to target gas can be broken down into two stages: the fast response at the beginning and the slow 'tail'. Those could be respectively assigned to the adsorption on low- and high-energy binding sites on the surface of functionalized graphene [102]. The time constants for the measurements under UV light, depicted in Figure 13, were obtained by fitting cures with a double exponential function, and are presented in **Table 1** below. Double exponential

fitting was applied to all sensor responses to $NO_2$, with only 40 ppb response for $ZrO_2$ being determined using a single exponential function, yielding t = 112 s.

**Table 1**. Response times $t_1$ and $t_2$ of $ZrO_2$- and Ag-modified graphene samples under UV light to 40, 100, 300 and 1000 ppb $NO_2$.

| | $ZrO_2$ | | | | Ag | | | |
|---|---|---|---|---|---|---|---|---|
| | 40 ppb | 100 ppb | 300 ppb | 1 ppm | 40 ppb | 100 ppb | 300 ppb | 1 ppm |
| $t_1$ (s) | – | 53 | 37 | 24 | 35 | 24 | 18 | 12 |
| $t_2$ (s) | – | 545 | 312 | 269 | 154 | 160 | 144 | 112 |

The time constants indicate that, under identical conditions, adsorption processes are faster for the Ag-modified sample. Further analysis shows that in the $ZrO_2$ measurement the response times were improved almost tenfold under UV light when compared to the measurement without the light assistance.

## 5.3 Graphene/$TiO_2$ heterostructures

The results covered in the previous section illustrate that continuous UV light illumination consistently enhanced sensor performance, often quite drastically. It played a crucial role in increasing gas response amplitudes and speeding up the signal recovery of the samples to the initial levels in the absence of the target gas. This synergistic effect between graphene surface functionalization and illumination requires further investigation and optimization for improved sensor performance. The experiments detailed below were conducted using a $TiO_2$-decorated graphene sensor. The $TiO_2$ sample was measured in parallel with $ZrO_2$ and Ag samples during gas sensitivity measurements and exhibited similar behavior and improvement under UV light. Compared to the heavier 4d-element Zr, $TiO_2$ has a smaller bandgap (3.2 eV for $TiO_2$ [75] and 5.0 eV for $ZrO_2$ [103]). Titanium oxides with lower valences could play a significant role in improving the sensitivity of gas sensors since they have lower band gaps and allow electron-hole pairs to be productively excited by the light [41]. Optical excitation of $TiO_2$ by UV wavelengths below 390 nm (corresponding to its bandgap) is possible, with photogenerated charge carriers potentially altering the chemical reactivity of the oxide surface [104].

Similar to the materials discussed in the preceding section, the $TiO_2$-coated graphene samples underwent analysis using Raman spectroscopy (Figure 14). Following the completion of all PLD cycles and gas measurements, SEM images from the samples were also captured.

Only a few defects were present in pristine graphene before PLD process (no visible D-peak at 1350 $cm^{-1}$). Analogously to the previously described samples, the pristine graphene was characterized as single-layered based on the G and 2D band peak positions (1590 $cm^{-1}$ and 2690 $cm^{-1}$, respectively) and their intensity ratio (ca 1:3).

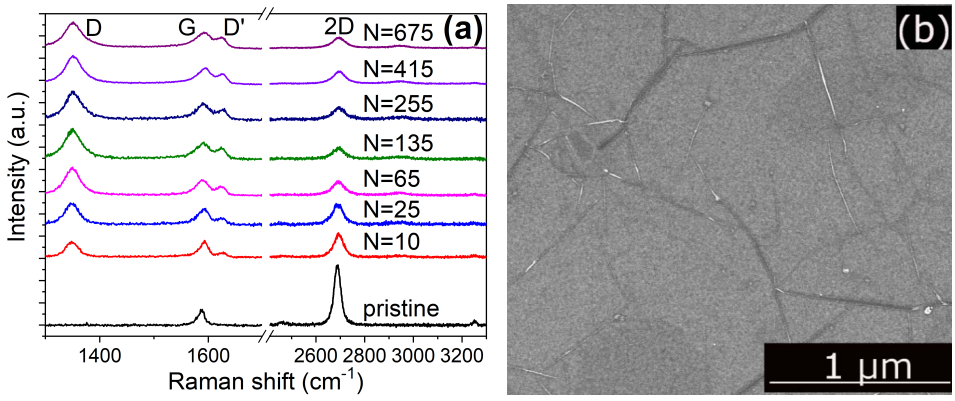


**Figure 14**. (a) Raman shift and (b) SEM image of a $TiO_2$-functionalized graphene. N signifies the number of used PLD laser impulses. Reprinted from **Paper III** under CC-BY 4.0 license.

The deposition of $TiO_2$ causes the appearance of defect-related D- and D'-peaks in the graphene Raman spectrum, while the intensity of the 2D band decreases. Subsequent Raman spectra exhibit a pattern similar to that of the $ZrO_2$-modified sample, with a slowdown in the broadening of the peaks after a couple of PLD cycles, unlike the case of Ag. The ratio of D and G band intensities changed from 1.25 (N = 10) to approximately 1.75 (N ≥ 135).

SEM image in Figure 14b was taken after the final deposition cycle (N = 675), displaying uniform coverage of the graphene surface by the granular oxide structure, similar to $ZrO_2$.

Figure 15a displays the XPS spectrum of a Gr/$TiO_2$ sample. Even though TiN was used as a PLD target material, the tested material turned out to be $TiO_2$ on top of graphene, as the lines corresponding to Ti, O, C, Si (substrate) and Au (metallic contacts) can be seen. Oxidation of a thin deposited layer in the ambient air is the most probable cause of the change.

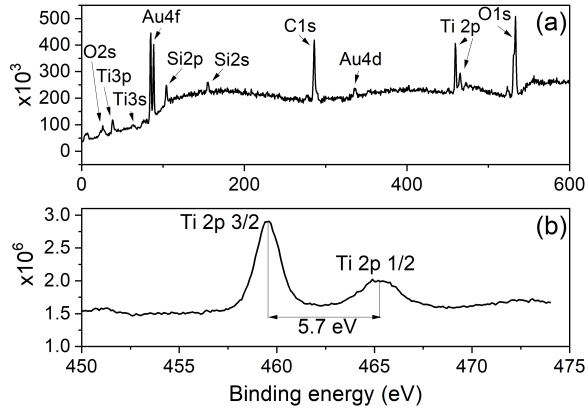


**Figure 15**. (a) XPS spectrum of $TiO_2$-coated graphene on Si/$SiO_2$ substrate with Au electrodes; (b) Ti2p spectrum. Reprinted from **Paper III** under CC-BY 4.0 license.

The symmetric peak for Ti2p is commonly expected in the XPS spectrum of $TiO_2$, which is confirmed by Figure 15b. The spin-orbit splitting of the Ti2p peak gives a value close to 5.7 eV, which is characteristic to the $TiO_2$. This confirms that the deposited material is mainly titania in $Ti^{4+}$ form.

XRF was used to confirm the absence of TiN on top of graphene: measurement showed mass areal density of 0.74 mg/cm$^2$ for Ti and 0.00 mg/cm$^2$ for nitrogen (measured after the last PLD cycle). The thickness of the $TiO_2$ was estimated to be 3.1 nm (assuming the $TiO_2$ density of 4.0 ± 0.2 g/cm$^3$, an average between rutile and anatase [105]). A similar conclusion was drawn from the ellipsometry data, with $TiO_2$ thickness calculated to be 6.2 ± 0.4 nm at 51% porosity. Using the gained data, the $TiO_2$ growth rate for PLD was estimated at 4.6 pm per laser pulse.

The elemental mapping of titanium dioxide on top of graphene and $Si/SiO_2$ substrate was also performed using energy dispersive X-ray spectroscopy. The uniform distribution of all the main components (Ti, C, Si, and O), as well as the SEM image of the scanned area, could be seen in Figure 16.

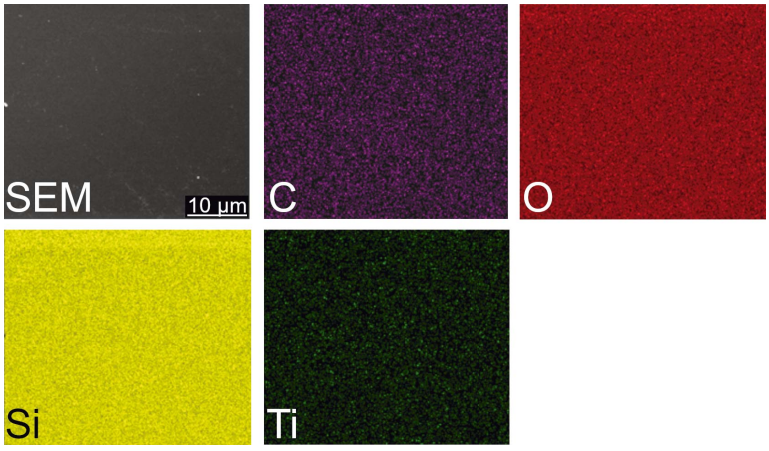


**Figure 16**. An elemental mapping analysis of the graphene/$TiO_2$ structure on top of the $Si/SiO_2$ substrate. An electron image of the scanned area and the distribution of constituent elements (C, O, Si and Ti) are shown. Reprinted from **Paper III** under CC-BY 4.0 license.

Quazi-two-dimensional DFT calculations were conducted to simulate graphene-$TiO_2$ interaction and adsorption of $NO_2$ gas on top of Gr/$TiO_2$ structure. Vienna *ab initio* simulation package (VASP) program package was used together with the potential projector augmented-wave (PAW) method and PBEsol functional approach with DFT-D3 corrections. Charge distribution in the system was analyzed using the Bader method.

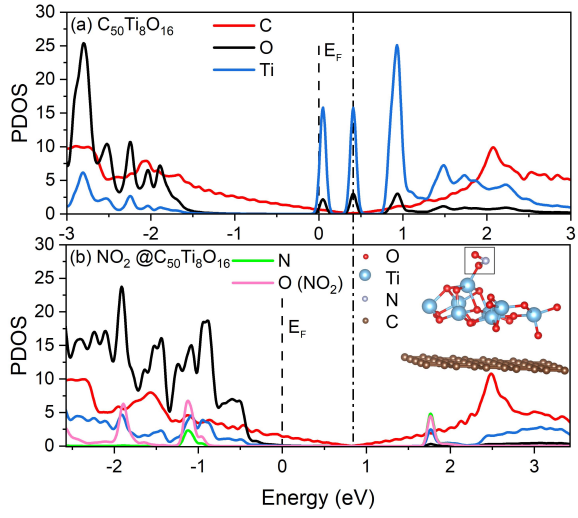


**Figure 17**. Partial densities of the states of (a) $Ti_8O_{16}C_{50}$ and (b) $NO_2$@$Ti_8O_{16}C_{50}$ complexes. Dashed lines mark the position of the Fermi level, while the position of the minima of PDOS of the carbon subsystem is shown using the dot-dashed line. In the inset of the lower panel, a schematic view of the ground state geometric structure of the complex $NO_2$@$Ti_8O_{16}C_{50}$ is shown. Data obtained using a **k**-mesh 25 × 25 × 1. Reprinted from **Paper III** under CC-BY 4.0 license.

First, the ground states of the $Ti_8O_{16}C_{50}$ cluster were determined, with the graphene sheet and layer of $TiO_2$ in a box, and added isolated $NO_2$ molecule in the same box. Carbon atoms were all fixed in the c-direction, while all Ti, N, and O atoms were fully relaxed during geometry optimization. Next, the ground state of the complex $NO_2$@$Ti_8O_{16}C_{50}$ was determined, and the final relaxed structure is presented in the inset of Figure 17.

The lattice parameters were 12.2, 12.2, and 34.3 Å. An energy equal to 2.65 eV was obtained for $NO_2$ adsorption on the $Ti_8O_{16}C_{50}$ cluster when a chemical bond formed between the oxygen belonging to the adsorbate and one of the Ti atoms. Similar energies are estimated for $NO_2$ adsorbed on graphene defects and impurities, but it is much higher than the value ranging between 0.055–0.067 eV for pristine graphene. It was established that electron charge transfer from the titanium and carbon subsystems to the adsorbate and oxygen subsystems takes place, and could happen both during the formation of the $Ti_8O_{16}C_{50}$ complex and the adsorption of $NO_2$. As a result of the adsorption process, the partial density of the electronic states (PDOS) of the carbon subsystem increases at the Fermi level. The PDOS of all atomic subsystems of the considered complexes is shown in Figure 17.

A band diagram of the p-doped graphene and $TiO_2$ is presented in Figure 18, separately and as a combined system. During the formation of the $Ti_8O_{16}C_{50}$ structure, Fermi levels ($E_F$) of the components align.

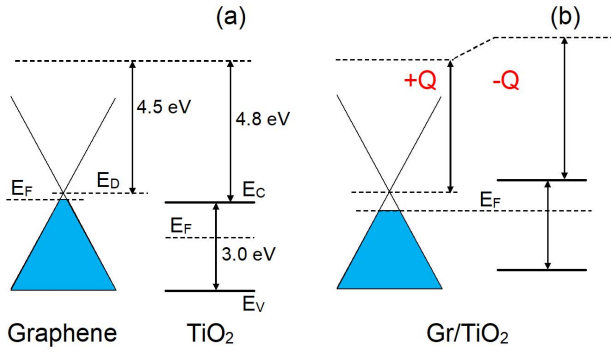


**Figure 18**. Band diagram of the p-doped graphene and thin $TiO_2$ layer (a) separately and (b) as a combined system. $E_F$ is the Fermi level, $E_D$ is the Dirac point energy of graphene (4.5 eV below the vacuum level), and $E_C$ and $E_V$ are the energies of conduction band minimum and valence band maximum, respectively. The charge transferred between the subsystems in the combined system is denoted by Q. Reproduced from **Paper III** under CC-BY 4.0 license.

In ambient air the valence band of the graphene is not fully occupied since the molecules adsorbed on it withdraw electrons, making graphene p-type. As it was established from DFT calculations results presented above, some of the electron charge transfer also happens during $Ti_8O_{16}C_{50}$ complex formation, so the valence band maximum of the graphene/$TiO_2$ system is located even lower.

The transconductance curves of a graphene sensor before and after the deposition of the $TiO_2$ are shown in Figure 19. The sample was annealed for two hours in dry nitrogen at 150 °C to reduce the Fermi level shift induced by oxygen and water molecules adsorbed from ambient air.

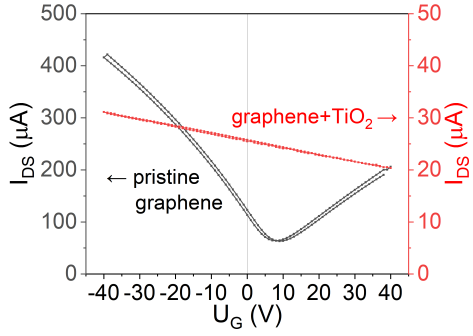


**Figure 19**. Transconductance before and after $TiO_2$ deposition onto graphene. Reprinted from **Paper III** under CC-BY 4.0 license.

A V-shaped curve, typical for the pristine graphene, shows the Dirac point at the gate voltage $U_G$ = 8 V and the field effect hole mobility of 2035 $cm^2/Vs$ at $U_G$ = 0 V. The mobility dropped drastically, to 29 $cm^2/Vs$, after the deposition of ~0.6 nm of $TiO_2$, and the Dirac point moved out of the measurement scale. In general, for measured samples, the mobility was in the range of 1000–4000 $cm^2/Vs$ before and 25–30 $cm^2/Vs$ after $TiO_2$ deposition.

Initially, the impact of illuminating graphene's surface with three different wavelengths (546, 436, and 365 nm) was investigated (see Figure 20). Each wavelength was applied for an hour before switching to the next one, aiming to observe their influence on the electrical signal of $TiO_2$-modified graphene.

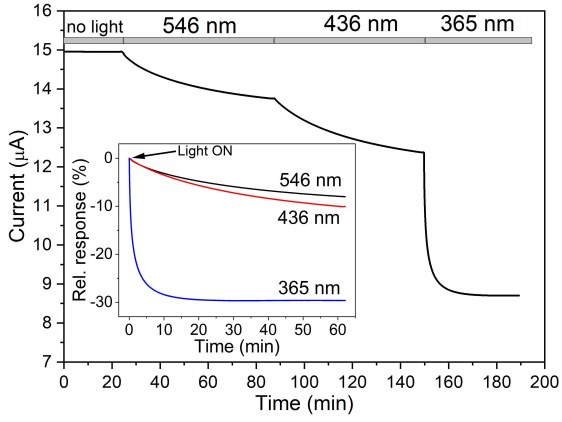


**Figure 20**. Changes in the $TiO_2$-decorated graphene sensor signal under illumination by 536, 436 and 365 nm light. Photon flux ($3.7\times10^{20}$ photons/$m^2$·s) was kept constant during the entire experiment for all wavelengths. Inset shows relative change of signal in a sample under three used wavelengths. Reprinted from **Paper III** under CC-BY 4.0 license.

At first, the sample was exposed to a continuous flow of synthetic air (RH = 20%). When the signal stabilized over an extended period, 546 nm light was directed onto the graphene located between two metallic electrodes. A noticeable but gradual decrease in the signal was observed, and the signal continued to decrease even after 60 minutes. After an hour, the wavelength was switched to 436 nm by changing an optical filter in front of the lamp, resulting in a slightly faster decline in electrical current. The behavior of the signal under 436 nm was quite similar to that under 546 nm light. After another hour, UV light with a wavelength of 365 nm was applied following an optical filter change. This change caused a rapid drop in the signal, and a stable plateau was reached at 8.75 μA. The effect of 365 nm UV light was much stronger compared to 546 nm and 436 nm, causing a 30% signal change compared to a 10% change. For 436 nm and 546 nm light, the light quanta have energies of 2.84 eV and 2.27 eV, which is smaller than the $TiO_2$ bandgap (>3 eV [105]). The electrical current decrease after exposure to UV light is consistent with previous graphene/$TiO_2$ composite investigations, and this process is expected to create free electrons and holes as potential active centers on the material's surface [63]. As mentioned in the introductory part of this work, the decrease in conductivity under illumination is most likely driven by the desorption of contaminants on the graphene surface, such as water and organic molecules, resulting in a decrease of predominant hole charge carrier numbers [106].

The photogeneration of electron-hole pairs in graphene happens on the absorption of light:

$$h\nu \rightarrow e^{-}_{(h\nu)} + h^{+}_{(h\nu)}$$

Water, oxygen and other adsorbed molecules can interact with created charge carriers, recombining and leaving the sensor surface [8]:

$$h^{+}_{(h\nu)} + O^{-}_{2(ads)} \rightarrow O_{2(gas)}$$

The counterweight to this process is the adsorption of molecules like oxygen from the synthetic air running through the measurement chamber [37]:

$$O_{2(gas)} + e^{-}_{(h\nu)} \rightarrow O^{-}_{2(h\nu)}$$

However, desorption appears to be predominant until equilibrium is established at a lower electrical current level. Thus, both the photodesorption of adsorbed gas molecules and the photogeneration of electron-hole pairs in graphene contribute to the changes in the conductivity [107, 108]. The 365 nm light has a stronger influence on the sample behavior compared to other tested wavelengths. Other preliminary measurements with various $TiO_2$-modified graphene gas sensors showed similar dependence, leading to the choice of the 365 nm wavelength in the light-enhanced gas sensitivity measurements in this work.

As the next step in the research, 300 ppb $NO_2$ was introduced into the test chamber during measurement identical to the one in Figure 20. The effect of illumination on gas response was compared for 536, 436 and 365 nm light. The experiment was performed at RH = 20%, and the sample was held in synthetic air before the start of the experiment (Figure 21). $NO_2$ was introduced into a chamber for 30 minutes for each wavelength used.

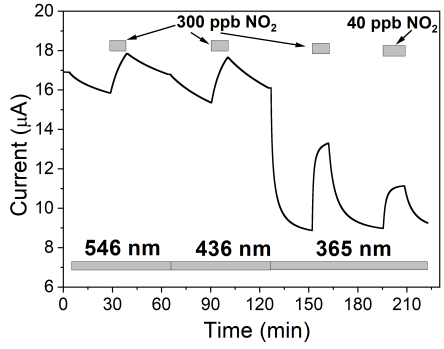


**Figure 21**. Response of $TiO_2$-modified graphene to 300 ppb $NO_2$ under illumination by 546 nm, 436 nm and 365 nm light. Measurement was performed in synthetic air at room temperature (RH = 20%). Reprinted from **Paper III** under CC-BY 4.0 license.

Initially, a $TiO_2$-modified graphene sample was placed in the measurement chamber in synthetic air (RH = 20%) until the electrical signal stabilized. Next, the 546 nm light was then turned on for an hour, and 300 ppb $NO_2$ was added to the carrier gas for gas response measurement. A 10% signal change was registered,

with partial signal recovery under 546 nm light. The same procedure was repeated with 436 nm light, resulting in a similar response. Switching to the 365 nm light caused a much stronger decrease in the electrical signal, reaching a similar ≈8.5 μA level as in the previous experiment.

In Figure 21, the gas response to 300 ppb $NO_2$ under 365 nm light is significantly higher compared to 546 nm and 436 nm wavelengths (50% vs. 10% change) during a 30-minute cycle. It should be noted that the signal is much closer to saturation under 365 nm light while reacting to $NO_2$. After the sample's signal recovered in synthetic air under 365 nm light, 40 ppb of $NO_2$ was introduced into the chamber. A clear response to lower $NO_2$ concentration was registered, on par with responses to 300 ppb under other wavelengths. Light absorption by graphene could not be the cause of the substantial difference between UV and visible light effect, as it should be covering the wide range from far infrared to UV [109]. The prospect of a direct excitation of the nitrite anion $NO_2^-$, which could be formed when $NO_2$ attaches to the $TiO_2$/graphene surface, was found to be negligible because of the small absorption cross-section of only about 20 $M^{-1}cm^{-1}$ [110]. $TiO_2$ pigment, on the other hand, strongly absorbs UV radiation above 370 nm, whereas photoinduced charge carriers can both reduce $NO_2$ and oxidize $Ti^{3+}$ or $NO_2^-$ [105].

From fitting the Figure 21 curves with graphene gas sensor $NO_2$ responses under 546, 436, and 365 nm light, response times were obtained (Table 2). Gas response under 365 nm light is significantly faster when compared to the other wavelengths. While 546 and 436 nm data could be fit using a single exponential, a double exponential was required for 365 nm. It might signify the fact that adsorption might happen at the sites with different adsorption energy – while some sites bond with $NO_2$ molecules easily, other processes have higher energy barriers, thus signal growth continues slowly after the initial fast rise.

**Table 2**. Response times of graphene/$TiO_2$ to 300 ppb $NO_2$ under 546, 436 and 365 nm light.

| | 546 nm | 436 nm | 365 nm |
|---|---|---|---|
| $t_1$ (s) | 1662 | 1282 | 89 |
| $t_2$ (s) | – | – | 506 |

The 365 nm light has a more pronounced positive impact on the recovery phase after exposure to $NO_2$. In the absence of new $NO_2$ molecules in the test chamber, UV light speeds up signal recovery by facilitating the removal of adsorbed $NO_2$ molecules from the sample surface. The results suggest the usefulness of UV light as a surface cleaning mechanism, which 'refreshes' the state of the sensing layer even when the sensor is not continually exposed to UV light. Both experiments involving three different wavelengths highlight that only 365 nm light surpasses a critical threshold, mitigating a characteristic slow signal drift in synthetic air. Under UV light, substantial changes in the measured signal occur within the first

few seconds following the application of light or a change in gas composition. Moreover, it significantly amplifies the gas response to $NO_2$, especially at low gas concentrations.

To further explore the positive effect of 365 nm light, gas responses of $TiO_2$-modified graphene to various $NO_2$ concentrations were measured with and without 365 nm light illumination, as seen in Figure 22. The measurement was conducted at room temperature using synthetic air as a carrier gas (RH = 20%) with $NO_2$ concentrations ranging from 40 ppb to 1 ppm.

The inset graph of Figure 22 illustrates the response of unmodified pristine graphene to 4 ppm $NO_2$. It shows the unresponsiveness of pristine graphene to 4 ppm $NO_2$, and the gas response improvement achieved by UV illumination, when the sample becomes to some extent sensitive to $NO_2$.

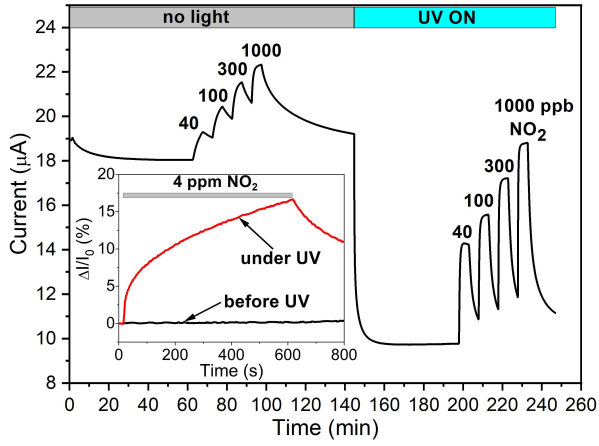


**Figure 22**. Response of a $TiO_2$-modified graphene to $NO_2$ concentrations ranging from 40 to 1000 ppb (room temperature, synthetic air, RH = 20%). Measurement was performed both with and without continuous UV illumination (λ = 365 nm). The inset shows a response of unmodified pristine graphene to 4 ppm $NO_2$. Reprinted from **Paper III** under CC-BY 4.0 license.

The PLD-modified graphene sample was held in synthetic air for over an hour to get a stable electrical signal, and then a series of $NO_2$ injections with concentrations between 40 to 1000 ppb were introduced into the measurement chamber, each for 5 min (see Figure 22, between 62 and 102 min). Between the changes in $NO_2$ concentrations, the sample was exposed to synthetic air (RH = 20%) for 5 min, leading to a partial signal recovery. In the recovery phase after contact with 1 ppm $NO_2$, the signal did not fully return to the initial level after a longer period of time, indicating that a certain percentage of $NO_2$ gas molecules remained adsorbed on the graphene surface. As observed in prior experiments with 365 nm light, here the electrical signal change also occurred rapidly in the first minutes after illumination began, at 144 min. A roughly 50% signal drop was recorded, stabilizing at a new level of 10 μA.

Under the UV light, the same $NO_2$ measurement was repeated. UV illumination significantly enhances the sensing capability of the graphene sample. In the case of 1 ppm gas response to $NO_2$, the increase in response goes from 24% (no UV) to 93% (under UV light). A change exceeding 40% is observed with 40 ppb $NO_2$ (approximately 10% in the dark), and even lower concentrations could be detected with $TiO_2$-modified graphene. The measurement in Figure 22 demonstrates that recovery under 365 nm light is rapid, but the signal is unable to reach initial levels within 5 minutes.

A single exponential function was used to approximate the response and recovery curves in Figure 22, and parameters are presented in Table 3 and in Figure 23.

**Table 3**. Relative response amplitudes and response/recovery characteristic times.

| $NO_2$ conc. (ppb) | Dark | | | UV | | |
|---|---|---|---|---|---|---|
| | $(G-G_{air})/G_{air}$ (%) | $t_{in}$ (s) | $t_{out}$ (s) | $(G-G_{air})/G_{air}$ (%) | $t_{in}$ (s) | $t_{out}$ (s) |
| 40 | 10 | 256 | 1317 | 46 | 24 | 103 |
| 100 | 14 | 145 | 534 | 57 | 18 | 97 |
| 300 | 20 | 97 | 295 | 73 | 12 | 102 |
| 1000 | 24 | 42 | 196 | 88 | 5.4 | 90 |

For the lowest $NO_2$ concentration used, 40 ppb, response times of 256 s and 24 s were obtained, for measurement in the dark and under UV light, respectively. Faster adsorption times under UV light could be once again assigned to effect of surface cleaning, where competing gas molecules are being removed from the surface of the sensor, freeing adsorption sites there.

Analyzing the recovery times, fitting resulted in the times between 1300 and 196 seconds for the measurement without UV light, but under UV light all the recovery times were in the range of $96 \pm 6$ s, regardless of $NO_2$ concentration measured. Also, based on the data collected on $NO_2$ sensitivity of the graphene/$TiO_2$ sensor and the relatively low measurement noise, the limit of detection was estimated to be at 0.03 ppb, and the sensitivity at 1%/ppb under UV light at room temperature.

In the Langmuir model where adsorbates on the homogeneous surface are not interacting between themselves, it would be expected that the recovery speed will only depend on the activation energy of desorption, but data from the measurement without UV light shows faster times for higher gas concentrations (Figure 23b). Interactions between adsorbates might be the key reason behind a faster desorption rates at a higher sensor surface coverage, caused by lower binding energies of the adsorbents [111]. Under UV light, the desorption energy barrier is crossed with help of the energy from the adsorbed light, leading to fairly similar desorption rates regardless of the gas concentration.

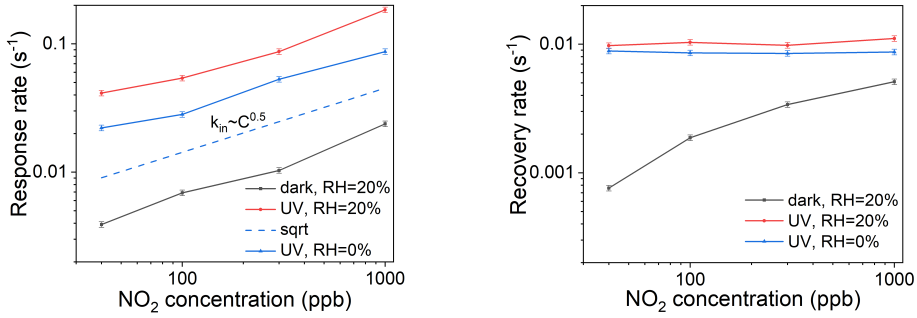


**Figure 23**. Dependence of the a) response and b) recovery rates on $NO_2$ concentration.

Both gas response and conductivity of the Gr/$TiO_2$ structure are affected by the laser deposition (thickness of the deposited material), and the effect is demonstrated in Figure 24. Each PLD sequence improved the relative responses of the sensor to $NO_2$ until 0.6 nm of titania was deposited, a value close to the single-layer $TiO_2$ thickness $d$ = 0.7 nm [112]. All following depositions caused a decrease of the gas response.

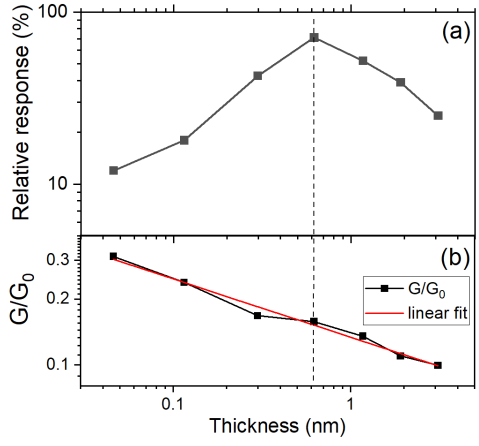


**Figure 24**. Dependence of the relative response to 300 ppb of $NO_2$ (a), and the normalized conductance $G/G_0$ ($G_0$ is the conductance of the sample before PLD) on the thickness of the deposited $TiO_2$ layer (b). Reprinted from **Paper III** under CC-BY 4.0 license.

In the case of the electrical conductance, starting with the first deposition, a decrease was registered, according to the power law $G \sim d^{0.27}$. It is caused by the increased number of defects in the graphene lattice caused by the PLD. This effect is strongly sublinear as previously deposited material acts as a shield, protecting the graphene lattice from further modification by the PLD plasma plume.

Figure 25 displays the long-term stability and repeatability of a $TiO_2$/graphene sensor responses to $NO_2$, an incredibly important qualities of a gas sensor. For over 2 years, the responses to $NO_2$ concentrations in the 40 ppb to 1 ppm range remained stable and repeatable even without preconditioning such as heating in the inert gas or vacuum.

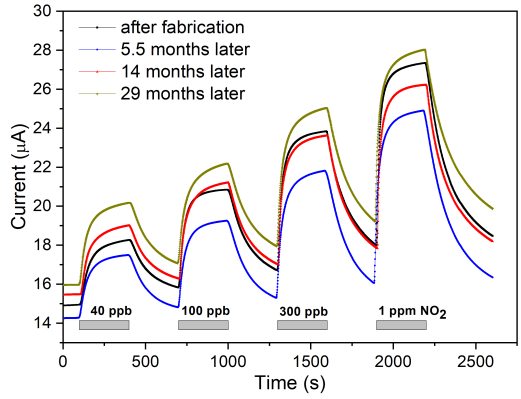


**Figure 25**. Repeatability and stability of a $TiO_2$/graphene sensor signal and gas responses during 29 months. Reprinted from **Paper III** under CC-BY 4.0 license.

The same sample was used in all the experiments, and during the long breaks between the tests sample was held in a laboratory room without special controls over humidity and temperature. Signal's baseline variations might be explained by the seasonal changes, as the changes were not monotonous in one direction. At the same time, gas response amplitudes were quite similar regardless of the month, with variations under 10%, suggesting great stability of the sample.

The functionalization of pristine graphene with $TiO_2$, as well as with $ZrO_2$ and Ag, considerably enhanced the amplitudes of gas response to $NO_2$. Responses to other potentially harmful gases ($NH_3$, CO, $SO_2$) were measured using the same $TiO_2$-graphene sample, and the results are depicted in Figure 26. Also, the cross-sensitivity to the relative humidity changes was measured. Signal changes caused by $NO_2$ turned out to be more prominent than humidity level variations, but at the same time measurements reflected that response amplitudes to $NO_2$ depend somewhat on RH level. Low concentrations of $NO_2$ measured in humid air gave higher responses compared to the measurements in dry air.

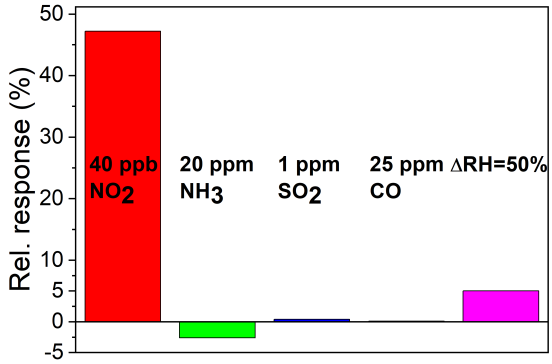


**Figure 26**. Responses of $TiO_2$-modified graphene to different pollutant gases and humidity level. change. Reprinted from **Paper III** under CC-BY 4.0 license.

A signal change over 40% was measured for 40 ppb $NO_2$ for graphene with PLD-transferred $TiO_2$. However, responses to much higher concentrations of $NH_3$, $SO_2$, CO, and water vapor were all below 5%. CO measurement showed no signal changes with gas concentrations as high as 25 ppm. Obtained results demonstrate the tendency of $NO_2$ to interact with a chosen set of dopants, but also encourage testing different compounds for obtaining selectivity to a specific gas. Similar results with high sensitivity to $NO_2$ (and NO) and low sensitivity towards many other gases were achieved with Si-doped graphene nanosheets [7]. On the other hand, the titanium dioxide/graphene biased field effect transistors achieved a great sensitivity to 25 ppm $NH_3$ [113], confirming that the device fabrication method plays a significant role in the performance of the gas sensor.

# 6. CONCLUSIONS

In this work, the light irradiation effect on the gas sensing properties of the graphene-based gas sensors was investigated. Both pristine single-layer CVD graphene and PLD-modified graphene structures were used for the detection of oxidizing gases, $NO_2$ and $O_2$.

The results demonstrate that UV light (365 and 300 nm) has a beneficial effect on the oxygen sensitivity of pristine graphene in ambient conditions at room temperature. It was found that the UV light irradiation caused the desorption of oxygen and water molecules from the surface of graphene, leading to the decrease of p-type conductivity and the creation of active unoccupied adsorption sites. Gas responses of the pristine graphene to the 21% change in oxygen concentration, that were practically absent in the dark (relative response below 0.1%), became substantial under UV light (> 25% response), and were reversible.

Pristine CVD graphene was also almost insensitive in respect to $NO_2$ without the UV assistance, also showing slow reaction kinetics. Therefore, graphene functionalized with zirconium and titanium dioxide nanolayers and silver nanoparticles was investigated next. In general, for $ZrO_2$ and Ag, the sensitivity increased in proportion to the amount of the deposited material up to a thickness of several nanometers. For $TiO_2$, the optimal thickness was established to be at 0.6 nm, which is comparable with the thickness of $TiO_2$ monolayer.

The improved sensitivity of the functionalized sensors was assigned to the creation of the new adsorption centers located on the surface of the laser-deposited nanomaterials. For the graphene/$TiO_2$ heterostructure, an efficient charge transfer between the graphene and the adsorbed $NO_2$ molecules happens, the latter presumably adsorbed at Ti cations. Thus, the $TiO_2$ layer acts as a receptor, while graphene is an electronic signal transducer.

As in the case of pristine graphene, the PLD-modified graphene structures also benefitted from the application of mild UV light (365 nm, 0.2 mW/mm$^2$). The results with the graphene/$TiO_2$ sensors indicated that the kinetics of the illuminated sensors had become faster roughly by an order of magnitude. For 40 ppb and 1 ppm of $NO_2$, the respective measured response times were between 24 and 5 s, while the recovery times were in the region of 100 s. Gas responses to 40 ppb $NO_2$ increased significantly as well, going from 10% (dark) to 40% (under UV light). For graphene modified with $ZrO_2$- and Ag, similarly measured gas responses to $NO_2$ reached 7–8% at 40 ppb and 20–30% at 1 ppm.

Using the experimental data from $NO_2$ measurements with graphene/$TiO_2$ at room temperature under UV light, the gas sensitivity and the limit of detection were estimated to be 1%/ppb and 0.03 ppb, respectively. Selectivity of graphene/$TiO_2$ heterostructure to $NO_2$ was also demonstrated: relative responses to other polluting gases at high concentrations (CO, $SO_2$, and $NH_3$ in the 1–25 ppm range) were significantly lower (< 5%) compared to the results achieved with $NO_2$ concentrations in the range of 40 ppb. Additionally, the graphene/$TiO_2$ heterostructures had a low (< 5%) cross-sensitivity to humidity.

The graphene/$TiO_2$ sensor demonstrated excellent long-term stability and repeatability of the gas responses. During almost a 3-year period, $NO_2$ measurements at concentrations ranging between 40 ppb to 1 ppm were performed under UV light repeatedly, without any special sample preconditioning. The results showed that the sensitivity changed by less than 10% over that time.

The effect of the visible light at wavelengths 436 and 546 nm on $NO_2$ gas response was compared to that of 365 nm UV light. A 50% gas response to 300 ppb of $NO_2$ was recorded under UV light with graphene/$TiO_2$, while under visible light same measurement resulted only in a 10% change. Concurrently, the response and recovery times under the UV light improved up to 10 times.

To conclude, graphene-based gas sensors have been tested in this work, and they exhibited great potential to be used for the environmental monitoring of $NO_2$. A further development of this research could be an incorporation of multiple graphene-based gas sensors, modified by the carefully chosen PLD materials, and light irradiation, into a united system aimed at the detection of a wider range of polluting gases.

# SUMMARY IN ESTONIAN

## Grafeenil põhinevad ja UV-valgusega aktiveeritud oksüdeerivate gaaside sensorid

Käesolevas töös on uuritud valguse mõju 2-mõõtmelisel materjalil – grafeenil – põhinevatele gaasisensoritele. Töös kasutati aurufaasist keemilise sadestusega valmistatud grafeeni, mida nii algolekus kui ka funktsionaliseeritud kujul rakendati oksüdeerivate gaaside (lämmastikdioksiidi ja hapniku) detekteerimiseks õhus.

Töö esimese osa tulemused demonstreerivad UV-valguse (300 ja 365 nm) aktiveerivat mõju hapnikumolekulide detekteerimisele. Leiti, et UV-kiirgus põhjustas grafeeni pinnale adsorbeerunud hapniku ja vee molekulide desorptsiooni, mis viis sensorite p-tüüpi juhtivuse vähenemiseni ja tekitas (vabastas) aktiivseid adsorptsioonitsentreid. Algselt tundetud sensorid (suhtelise kostega alla 0,1%) näitasid valguse mõju all enam kui 25%-list signaali muutust hapniku osakaalu 21% muutumisel õhus. UV-valgus kiirendas oluliselt ka sensorite koste- ja taastumiskiirusi ning signaalide muutused järgisid Langmuiri seadust.

Algse vähedefektse grafeeniga sensorid olid praktiliselt tundetud ka lämmastikdioksiidile ja nende signaali dünaamika oli väga aeglane. Seetõttu uuriti järgnevalt tsirkoonium- ja titaandioksiidi nanokihtidega ning hõbeda nanoosakestega funktsionaliseeritud grafeeni. Lasersadestusega tekitatud nanokihtide teatud kriitilise paksuseni suurenes sensorite gaasitundlikkus proportsionaalselt sadestatud materjali hulgaga. Parimaid tulemusi saadi lämmastikdioksiidi detekteerimisel, kui grafeenile kantud titaandioksiidi kiht oli paksusega 0,6 nm, mis vastab selle materjali ühele aatomkihile.

Funktsionaliseeritud grafeeniga sensorite edendatud gaasitundlikkus omistati uute adsorptsioonitsentrite tekkimisele lisatud nanomaterjali pinnal. Grafeen/$TiO_2$ heterostruktuurides adsorbeeruvad oksüdeerivad gaasimolekulid $TiO_2$ pinnal, kusjuures toimub elektroni ülekanne grafeeni ja adsorbeerunud molekulide vahel. Niisiis, oksiidi kiht käitub nagu retseptor, samal ajal kui grafeen käitub nagu muundur, mille elektrijuhtivus muutub laenguülekande tagajärjel.

Funktsionaliseeritud grafeeniga sensorid aktiveeruvad samuti juba nõrga UV-valguse (365 nm, 0,2 $mW/cm^2$) mõju all. Registreeritud dünaamilisi gaasikosteid sobitati eksponentfunktsioonidega ja tulemusena leiti, et sensorite kineetika kiirenes valguse mõjul vähemalt suurusjärgu võrra. $NO_2$ kontsentratsioonidel 40 ppb kuni 1 ppm õhus olid valguse mõju all mõõdetud kosteajad vastavalt 24 kuni 5 sekundit ja taastumisajad ligikaudu 100 sekundit. Sensori signaali suhtelised muutused suurenesid samuti valguse mõjul, olles valguse puudumisel 10% ja valguse mõjul kuni 40% $NO_2$ kontsentratsioonil 40 ppb. Tsirkooniumdioksiidi ja hõbedaga funktsionaliseeritud sensorid näitasid 7–8% kosteid 40 ppb korral ja 20–30% kosteid 1 ppm korral.

Kasutades grafeen/$TiO_2$ sensorstruktuuride mõõteandmeid, arvutati sensorite detekteerimisläveks $NO_2$ gaasi korral 0,03 ppb. Samuti demonstreeriti selliste struktuuride selektiivsust, kuna teiste saastavate gaaside ($CO_2$, $SO_2$, $NH_3$) kosted

olid palju suuremate kontsentratsioonide korral oluliselt väiksemad $NO_2$ kostetest. Lisaks oli sellistele sensorstruktuuridele väga vähene mõju õhuniiskusel.

Oksiididega funktsionaliseeritud sensorstruktuurid olid ka väga hea stabiilsusega. Ligi 3-aastase perioodi kestel pisteliselt testitud grafeen/$TiO_2$ sensorite puhul leiti, et nende tundlikkus muutus selle aja jooksul vähem kui 10 protsenti.

Töös uuriti ka erinevate lainepikkustega valguse mõju grafeen/$TiO_2$ sensorite tundlikkusele. Selleks kasutati lisaks 365 nm lainepikkusele (UV) ka 436 nm ja 546 nm lainepikkusi (nähtav valgus). Kuna nähtava valguse mõju oli väike, siis järeldati, et sensorprotsesside võimendamisel ja kiirendamisel etendas olulist rolli $TiO_2$ kihis valguse neeldumisel tekkiv elektron-auk paar.

Kokkuvõtvalt, selles töös arendati grafeenil põhinevaid gaasisensoreid, mis võiksid leida kasutust keskkonnaseires lämmastikdioksiidi kontsentratsiooni tuvastamisel. Töö edasiarendusena oleks huvipakkuv kombineerida erinevaid grafeenile sadestatavaid materjale ning valgusega ergastamise režiime eesmärgiga arendada sensoreid laiema saastegaaside spektri tuvastamiseks.

# ACKNOWLEDGEMENTS

First and foremost, I would like to thank my supervisors, Raivo Jaaniso and Harry Alles, for all the help, encouragement and support during my PhD journey.

Also, my deepest gratitude to all my colleagues and friends in the Institute of Physics, including Tea Avarmaa, Indrek Renge, Paniz Vafaei, for their valuable advice and support. I am thankful to Margus Kodu for his advice and assistance in conducting the measurements, and Tauno Kahro for sharing his expertise regarding graphene.

Several programs and institutions supported me during the studies, and I would like to extend my gratitude to all of them.

I am grateful to all the friends and family members who showed their support and gave encouragement during the PhD years.

Finally, my sincere gratitude goes to my wife, Marta. Thank you for always supporting me, be that in Estonia, Finland or Sweden.

# REFERENCES


[1] K. S. Novoselov, "Electric Field Effect in Atomically Thin Carbon Films," *Science*, vol. 306, no. 5696, pp. 666–669, Oct. 2004, doi: 10.1126/science. 1102896.

[2] V. B. Mbayachi, E. Ndayiragije, T. Sammani, S. Taj, E. R. Mbuta, and A. U. Khan, "Graphene synthesis, characterization and its applications: A review," *Results Chem.*, vol. 3, p. 100163, Jan. 2021, doi: 10.1016/j.rechem.2021.100163.

[3] A. Chakraborthy, S. Nuthalapati, A. Nag, N. Afsarimanesh, Md. E. E. Alahi, and M. E. Altinsoy, "A Critical Review of the Use of Graphene-Based Gas Sensors," *Chemosensors*, vol. 10, no. 9, p. 355, Sep. 2022, doi: 10.3390/chemosensors 10090355.

[4] S. Dandeliya and S. Anurag, "Defected Graphene as Ammonia Sensor: Theoretical Insight," *IEEE Sens. J.*, vol. 19, no. 6, pp. 2031–2038, Mar. 2019, doi: 10.1109/JSEN.2018.2884971.

[5] S. Feng, Z. Lin, X. Gan, R. Lv, and M. Terrones, "Doping two-dimensional materials: ultra-sensitive sensors, band gap tuning and ferromagnetic monolayers," *Nanoscale Horiz.*, vol. 2, no. 2, pp. 72–80, 2017, doi: 10.1039/C6NH00192K.

[6] X. Tang, N. Mager, B. Vanhorenbeke, S. Hermans, and J.-P. Raskin, "Defect-free functionalized graphene sensor for formaldehyde detection," *Nanotechnology*, vol. 28, no. 5, p. 055501, Feb. 2017, doi: 10.1088/1361-6528/28/5/055501.

[7] F. Niu, Z.-W. Shao, H. Gao, L.-M. Tao, and Y. Ding, "Si-doped graphene nanosheets for NOx gas sensing," *Sens. Actuators B Chem.*, vol. 328, p. 129005, Feb. 2021, doi: 10.1016/j.snb.2020.129005.

[8] R. Kumar, X. Liu, J. Zhang, and M. Kumar, "Room-Temperature Gas Sensors Under Photoactivation: From Metal Oxides to 2D Materials," *Nano-Micro Lett.*, vol. 12, no. 1, p. 164, Dec. 2020, doi: 10.1007/s40820-020-00503-4.

[9] P. Sun *et al.*, "Photoinduced molecular desorption from graphene films," *Appl. Phys. Lett.*, vol. 101, no. 5, p. 053107, Jul. 2012, doi: 10.1063/1.4742147.

[10] V. Georgakilas *et al.*, "Functionalization of Graphene: Covalent and Non-Covalent Approaches, Derivatives and Applications," *Chem. Rev.*, vol. 112, no. 11, pp. 6156–6214, Nov. 2012, doi: 10.1021/cr3000412.

[11] Y.-H. Zhang *et al.*, "Improving gas sensing properties of graphene by introducing dopants and defects: a first-principles study," *Nanotechnology*, vol. 20, no. 18, p. 185504, May 2009, doi: 10.1088/0957-4484/20/18/185504.

[12] M. Kodu *et al.*, "Highly sensitive $NO_2$ sensors by pulsed laser deposition on graphene," *Appl. Phys. Lett.*, vol. 109, no. 11, p. 113108, Sep. 2016, doi: 10.1063/1.4962959.

[13] M. Kodu *et al.*, "Gas-Sensing Properties of Graphene Functionalized with Ternary Cu-Mn Oxides for E-Nose Applications," *Chemosensors*, vol. 11, no. 8, p. 460, Aug. 2023, doi: 10.3390/chemosensors11080460.

[14] D. J. Jarvis, G. Adamkiewicz, M.-E. Heroux, R. Rapp, and F. J. Kelly, *Nitrogen dioxide*. World Health Organization, 2010. Accessed: Nov. 18, 2021. [Online]. Available: https://www.ncbi.nlm.nih.gov/books/NBK138707/

[15] S. C. Pryor, P. Crippa, and R. C. Sullivan, "Atmospheric Chemistry," in *Reference Module in Earth Systems and Environmental Sciences*, Elsevier, 2015, p. B97801 24095489091776. doi: 10.1016/B978-0-12-409548-9.09177-6.

[16] World Health Organization: Geneva, "WHO global air quality guidelines. Particulate matter (PM2.5 and PM10), ozone, nitrogen dioxide, sulfur dioxide and

carbon monoxide," 2021, [Online]. Available: https://iris.who.int/ bitstream/ handle/10665/345329/9789240034228-eng.pdf
[17] D. Panda, A. Nandi, S. K. Datta, H. Saha, and S. Majumdar, "Selective detection of carbon monoxide (CO) gas by reduced graphene oxide (rGO) at room temperature," *RSC Adv.*, vol. 6, no. 53, pp. 47337–47348, 2016, doi: 10.1039/C6RA06058G.
[18] T. O. Wehling, M. I. Katsnelson, and A. I. Lichtenstein, "Adsorbates on graphene: Impurity states and electron scattering," *Chem. Phys. Lett.*, vol. 476, no. 4–6, pp. 125–134, Jul. 2009, doi: 10.1016/j.cplett.2009.06.005.
[19] A. C. Ferrari *et al.*, "Science and technology roadmap for graphene, related two-dimensional crystals, and hybrid systems," *Nanoscale*, vol. 7, no. 11, pp. 4598–4810, 2015, doi: 10.1039/C4NR01600A.
[20] N. F. Atta, A. Galal, and E. H. El-Ads, "Graphene – A Platform for Sensor and Biosensor Applications," in *Biosensors – Micro and Nanoscale Applications*, T. Rinken, Ed., InTech, 2015. doi: 10.5772/60676.
[21] A. A. Balandin *et al.*, "Superior Thermal Conductivity of Single-Layer Graphene," *Nano Lett.*, vol. 8, no. 3, pp. 902–907, Mar. 2008, doi: 10.1021/nl0731872.
[22] M. Pérez, J. Elías, M. Sosa, and M. Vallejo, "Hybridization bond states and band structure of graphene: a simple approach," *Eur. J. Phys.*, vol. 43, no. 4, p. 045401, Jul. 2022, doi: 10.1088/1361-6404/ac654e.
[23] Ponor, *Electronic band structure of graphene*, 2020. [Online]. Available: https://commons.wikimedia.org/wiki/File:Electronic_band_structure_of_graphene.svg
[24] D. R. Cooper *et al.*, "Experimental Review of Graphene," *ISRN Condens. Matter Phys.*, vol. 2012, pp. 1–56, Apr. 2012, doi: 10.5402/2012/501686.
[25] J. Eriksson, D. Puglisi, Y. H. Kang, R. Yakimova, and A. Lloyd Spetz, "Adjusting the electronic properties and gas reactivity of epitaxial graphene by thin surface metallization," *Phys. B Condens. Matter*, vol. 439, pp. 105–108, Apr. 2014, doi: 10.1016/j.physb.2013.11.009.
[26] P. L. Levesque *et al.*, "Probing Charge Transfer at Surfaces Using Graphene Transistors," *Nano Lett.*, vol. 11, no. 1, pp. 132–137, Jan. 2011, doi: 10.1021/nl103015w.
[27] A. K. Geim and K. S. Novoselov, "The rise of graphene," *Nat. Mater.*, vol. 6, no. 3, pp. 183–191, Mar. 2007, doi: 10.1038/nmat1849.
[28] F. Schedin *et al.*, "Detection of individual gas molecules adsorbed on graphene," *Nat. Mater.*, vol. 6, no. 9, pp. 652–655, Sep. 2007, doi: 10.1038/nmat1967.
[29] A. K. Geim, "Graphene: Status and Prospects," *Science*, vol. 324, no. 5934, pp. 1530–1534, Jun. 2009, doi: 10.1126/science.1158877.
[30] R. C. Sinclair, J. L. Suter, and P. V. Coveney, "Micromechanical exfoliation of graphene on the atomistic scale," *Phys. Chem. Chem. Phys.*, vol. 21, no. 10, pp. 5716–5722, Mar. 2019, doi: 10.1039/C8CP07796G.
[31] M. Gautam and A. H. Jayatissa, "Gas sensing properties of graphene synthesized by chemical vapor deposition," *Mater. Sci. Eng. C*, vol. 31, no. 7, pp. 1405–1411, Oct. 2011, doi: 10.1016/j.msec.2011.05.008.
[32] D. Wei, Y. Liu, Y. Wang, H. Zhang, L. Huang, and G. Yu, "Synthesis of N-Doped Graphene by Chemical Vapor Deposition and Its Electrical Properties," *Nano Lett.*, vol. 9, no. 5, pp. 1752–1758, May 2009, doi: 10.1021/nl803279t.
[33] Z. A. Van Veldhoven, J. A. Alexander-Webber, A. A. Sagade, P. Braeuninger-Weimer, and S. Hofmann, "Electronic properties of CVD graphene: The role of grain boundaries, atmospheric doping, and encapsulation by ALD," *Phys. Status Solidi B*, vol. 253, no. 12, pp. 2321–2325, Dec. 2016, doi: 10.1002/pssb.201600255.

[34] Md. W. K. Nomani *et al.*, "Highly sensitive and selective detection of $NO_2$ using epitaxial graphene on 6H-SiC," *Sens. Actuators B Chem.*, vol. 150, no. 1, pp. 301–307, Sep. 2010, doi: 10.1016/j.snb.2010.06.069.

[35] M. Acik *et al.*, "The Role of Oxygen during Thermal Reduction of Graphene Oxide Studied by Infrared Absorption Spectroscopy," *J. Phys. Chem. C*, vol. 115, no. 40, pp. 19761–19781, Oct. 2011, doi: 10.1021/jp2052618.

[36] S. Ramanavicius, A. Jagminas, and A. Ramanavicius, "Gas Sensors Based on Titanium Oxides (Review)," *Coatings*, vol. 12, no. 5, p. 699, May 2022, doi: 10.3390/coatings12050699.

[37] E. Espid and F. Taghipour, "UV-LED Photo-activated Chemical Gas Sensors: A Review," *Crit. Rev. Solid State Mater. Sci.*, vol. 42, no. 5, pp. 416–432, Sep. 2017, doi: 10.1080/10408436.2016.1226161.

[38] X. Tang *et al.*, "A Fast and Room-Temperature Operation Ammonia Sensor Based on Compound of Graphene With Polypyrrole," *IEEE Sens. J.*, vol. 18, no. 22, pp. 9088–9096, Nov. 2018, doi: 10.1109/JSEN.2018.2869203.

[39] W. Tian, X. Liu, and W. Yu, "Research Progress of Gas Sensor Based on Graphene and Its Derivatives: A Review," *Appl. Sci.*, vol. 8, no. 7, Art. no. 7, Jul. 2018, doi: 10.3390/app8071118.

[40] J. H. Kim, M. M. Haidari, J. S. Choi, H. Kim, Y.-J. Yu, and J. Park, "Facile Dry Surface Cleaning of Graphene by UV Treatment," *J. Korean Phys. Soc.*, vol. 72, no. 9, pp. 1045–1051, May 2018, doi: 10.3938/jkps.72.1045.

[41] M. Zhao *et al.*, "Room temperature $NH_3$ detection of Ti/graphene devices promoted by visible light illumination," *J. Mater. Chem. C*, vol. 5, no. 5, pp. 1113–1120, Feb. 2017, doi: 10.1039/C6TC04416F.

[42] B. Saruhan, R. Lontio Fomekong, and S. Nahirniak, "Review: Influences of Semiconductor Metal Oxide Properties on Gas Sensing Characteristics," *Front. Sens.*, vol. 2, p. 2, 2021, doi: 10.3389/fsens.2021.657931.

[43] T. O. Wehling *et al.*, "Molecular Doping of Graphene," *Nano Lett.*, vol. 8, no. 1, pp. 173–177, Jan. 2008, doi: 10.1021/nl072364w.

[44] C. Schiattarella *et al.*, "CVD transfer-free graphene for sensing applications," *Beilstein J. Nanotechnol.*, vol. 8, pp. 1015–1022, May 2017, doi: 10.3762/bjnano.8.102.

[45] G. Ko, H.-Y. Kim, J. Ahn, Y.-M. Park, K.-Y. Lee, and J. Kim, "Graphene-based nitrogen dioxide gas sensors," *Curr. Appl. Phys.*, vol. 10, no. 4, pp. 1002–1004, Jul. 2010, doi: 10.1016/j.cap.2009.12.024.

[46] L. Yang *et al.*, "Moisture-resistant, stretchable NOx gas sensors based on laser-induced graphene for environmental monitoring and breath analysis," *Microsyst. Nanoeng.*, vol. 8, no. 1, p. 78, Jul. 2022, doi: 10.1038/s41378-022-00414-x.

[47] T. Minami, S. Ochi, H. Nakai, T. Kinoshita, Y. Ohno, and M. Nagase, "Thermal desorption of structured water layer on epitaxial graphene," *AIP Adv.*, vol. 11, no. 12, p. 125012, Dec. 2021, doi: 10.1063/5.0075191.

[48] F. R. Bagsican *et al.*, "Adsorption energy of oxygen molecules on graphene and two-dimensional tungsten disulfide," *Sci. Rep.*, vol. 7, no. 1, p. 1774, May 2017, doi: 10.1038/s41598-017-01883-1.

[49] C. Melios *et al.*, "Effects of humidity on the electronic properties of graphene prepared by chemical vapour deposition," *Carbon*, vol. 103, pp. 273–280, Jul. 2016, doi: 10.1016/j.carbon.2016.03.018.

[50] C. W. Chen *et al.*, "Oxygen sensors made by monolayer graphene under room temperature," *Appl. Phys. Lett.*, vol. 99, no. 24, p. 243502, Dec. 2011, doi: 10.1063/1.3668105.

[51] X. Tang, M. Debliquy, D. Lahem, Y. Yan, and J.-P. Raskin, "A Review on Functionalized Graphene Sensors for Detection of Ammonia," *Sensors*, vol. 21, no. 4, Art. no. 4, Jan. 2021, doi: 10.3390/s21041443.

[52] C. Wang, Y. Wang, Z. Yang, and N. Hu, "Review of recent progress on graphene-based composite gas sensors," *Ceram. Int.*, vol. 47, no. 12, pp. 16367–16384, Jun. 2021, doi: 10.1016/j.ceramint.2021.02.144.

[53] A. Khort *et al.*, "High-performance selective $NO_2$ gas sensor based on In2O3–graphene–Cu nanocomposites," *Sci. Rep.*, vol. 13, no. 1, p. 7834, May 2023, doi: 10.1038/s41598-023-34697-5.

[54] M. G. Chung *et al.*, "Highly sensitive $NO_2$ gas sensor based on ozone treated graphene," *Sens. Actuators B Chem.*, vol. 166–167, pp. 172–176, May 2012, doi: 10.1016/j.snb.2012.02.036.

[55] T. Kuila, S. Bose, A. K. Mishra, P. Khanra, N. H. Kim, and J. H. Lee, "Chemical functionalization of graphene and its applications," *Prog. Mater. Sci.*, vol. 57, no. 7, pp. 1061–1105, Sep. 2012, doi: 10.1016/j.pmatsci.2012.03.002.

[56] G. Hong, Q.-H. Wu, J. Ren, C. Wang, W. Zhang, and S.-T. Lee, "Recent progress in organic molecule/graphene interfaces," *Nano Today*, vol. 8, no. 4, pp. 388–402, Aug. 2013, doi: 10.1016/j.nantod.2013.07.003.

[57] H. Y. Mao, Y. H. Lu, J. D. Lin, S. Zhong, A. T. S. Wee, and W. Chen, "Manipulating the electronic and chemical properties of graphene via molecular functionalization," *Prog. Surf. Sci.*, vol. 88, no. 2, pp. 132–159, May 2013, doi: 10.1016/j.progsurf.2013.02.001.

[58] B. H. Chu *et al.*, "Hydrogen detection using platinum coated graphene grown on SiC," *Sens. Actuators B Chem.*, vol. 157, no. 2, pp. 500–503, Oct. 2011, doi: 10.1016/j.snb.2011.05.007.

[59] D.-T. Phan and G.-S. Chung, "Characteristics of resistivity-type hydrogen sensing based on palladium-graphene nanocomposites," *Int. J. Hydrog. Energy*, vol. 39, no. 1, pp. 620–629, Jan. 2014, doi: 10.1016/j.ijhydene.2013.08.107.

[60] A. Gutés *et al.*, "Graphene decoration with metal nanoparticles: Towards easy integration for sensing applications," *Nanoscale*, vol. 4, no. 2, pp. 438–440, 2012, doi: 10.1039/C1NR11537E.

[61] B. Zu, B. Lu, Z. Yang, Y. Guo, X. Dou, and T. Xu, "Gas Adsorption Thermodynamics Deduced from the Electrical Responses in Gas-Gated Field-Effect Nanosensors," *J. Phys. Chem. C*, vol. 118, no. 26, pp. 14703–14710, Jul. 2014, doi: 10.1021/jp505279m.

[62] Q. Li *et al.*, "Nitrogen Dioxide Gas Sensor Based on Ag-Doped Graphene: A First-Principle Study," *Chemosensors*, vol. 9, no. 8, p. 227, Aug. 2021, doi: 10.3390/chemosensors9080227.

[63] Q. Wang *et al.*, "$TiO_2$-decorated graphenes as efficient photoswitches with high oxygen sensitivity," *Chem. Sci.*, vol. 2, no. 9, pp. 1860–1864, Aug. 2011, doi: 10.1039/C1SC00344E.

[64] H. Fei *et al.*, "Enhanced $NO_2$ Sensing at Room Temperature with Graphene via Monodisperse Polystyrene Bead Decoration," *ACS Omega*, vol. 4, no. 2, pp. 3812–3819, Feb. 2019, doi: 10.1021/acsomega.8b03540.

[65] L. Guo and T. Li, "Sub-ppb and ultra selective nitrogen dioxide sensor based on sulfur doped graphene," *Sens. Actuators B Chem.*, vol. 255, pp. 2258–2263, Feb. 2018, doi: 10.1016/j.snb.2017.09.021.

[66] A. Eckmann *et al.*, "Probing the Nature of Defects in Graphene by Raman Spectroscopy," *Nano Lett.*, vol. 12, no. 8, pp. 3925–3930, Aug. 2012, doi: 10.1021/nl300901a.

[67] W. Kassem, M. Tabbal, and M. Roumie, "Pulsed Laser Deposition of Tungsten Thin Films on Graphite," *Adv. Mater. Res.*, vol. 324, pp. 77–80, Aug. 2011, doi: 10.4028/www.scientific.net/AMR.324.77.

[68] K. Wang, "Laser Based Fabrication of Graphene," in *Advances in Graphene Science*, M. Aliofkhazraei, Ed., InTech, 2013. doi: 10.5772/55821.

[69] S. Rani, M. Kumar, S. Sharma, D. Kumar, and S. Tyagi, "Effect of Graphene in Enhancing the Photo Catalytic Activity of Zirconium Oxide," *Catal. Lett.*, vol. 144, no. 2, pp. 301–307, Feb. 2014, doi: 10.1007/s10562-013-1125-0.

[70] R. Ghanbari, R. Safaiee, M. H. Sheikhi, M. M. Golshan, and Z. K. Horastani, "Graphene Decorated with Silver Nanoparticles as a Low-Temperature Methane Gas Sensor," *ACS Appl. Mater. Interfaces*, vol. 11, no. 24, pp. 21795–21806, Jun. 2019, doi: 10.1021/acsami.9b00625.

[71] S. Rattan, S. Kumar, and J. K. Goswamy, "Gold nanoparticle decorated graphene for efficient sensing of $NO_2$ gas," *Sens. Int.*, vol. 3, p. 100147, 2022, doi: 10.1016/j.sintl.2021.100147.

[72] M. Zhao *et al.*, "High efficiency room temperature detection of $NO_2$ gas based on ultrathin metal/graphene devices," *RSC Adv.*, vol. 6, no. 87, pp. 84082–84089, 2016, doi: 10.1039/C6RA16863A.

[73] O. Ovsianytskyi, Y.-S. Nam, O. Tsymbalenko, P.-T. Lan, M.-W. Moon, and K.-B. Lee, "Highly sensitive chemiresistive $H_2S$ gas sensor based on graphene decorated with Ag nanoparticles and charged impurities," *Sens. Actuators B Chem.*, vol. 257, pp. 278–285, Mar. 2018, doi: 10.1016/j.snb.2017.10.128.

[74] E. A. Nunes Simonetti, T. Cardoso De Oliveira, Á. Enrico Do Carmo Machado, A. A. Coutinho Silva, A. Silva Dos Santos, and L. De Simone Cividanes, "$TiO_2$ as a gas sensor: The novel carbon structures and noble metals as new elements for enhancing sensitivity – A review," *Ceram. Int.*, vol. 47, no. 13, pp. 17844–17876, Jul. 2021, doi: 10.1016/j.ceramint.2021.03.189.

[75] D. O. Scanlon *et al.*, "Band alignment of rutile and anatase $TiO_2$," *Nat. Mater.*, vol. 12, no. 9, pp. 798–801, Sep. 2013, doi: 10.1038/nmat3697.

[76] M. Faraldos and A. Bahamonde, "Environmental applications of titania-graphene photocatalysts," *Catal. Today*, vol. 285, pp. 13–28, May 2017, doi: 10.1016/j.cattod.2017.01.029.

[77] Q. Zhang *et al.*, "Structure and photocatalytic properties of $TiO_2$-Graphene Oxide intercalated composite," *Chin. Sci. Bull.*, vol. 56, no. 3, pp. 331–339, Jan. 2011, doi: 10.1007/s11434-010-3111-x.

[78] Z. Ye *et al.*, "Excellent ammonia sensing performance of gas sensor based on graphene/titanium dioxide hybrid with improved morphology," *Appl. Surf. Sci.*, vol. 419, pp. 84–90, Oct. 2017, doi: 10.1016/j.apsusc.2017.03.251.

[79] M. Kodu *et al.*, "Graphene-Based Ammonia Sensors Functionalised with Sub-Monolayer $V_2O_5$: A Comparative Study of Chemical Vapour Deposited and Epitaxial Graphene †," *Sensors*, vol. 19, no. 4, p. 951, Feb. 2019, doi: 10.3390/s19040951.

[80] M. Shaik, V. K. Rao, M. Gupta, K. S. R. C. Murthy, and R. Jain, "Chemiresistive gas sensor for the sensitive detection of nitrogen dioxide based on nitrogen doped graphene nanosheets," *RSC Adv.*, vol. 6, no. 2, pp. 1527–1534, 2016, doi: 10.1039/C5RA21184K.

[81] A. Yurgens, N. Lindvall, J. Sun, Y. Nam, and Y. W. Park, “Control of the Dirac point in graphene by UV light,” *JETP Lett.*, vol. 98, no. 11, pp. 704–708, Feb. 2014, doi: 10.1134/S0021364013240211.
[82] C. Biswas *et al.*, “Negative and Positive Persistent Photoconductance in Graphene,” *Nano Lett.*, vol. 11, no. 11, pp. 4682–4687, Nov. 2011, doi: 10.1021/nl202266h.
[83] R. J. Chen *et al.*, “Molecular photodesorption from single-walled carbon nanotubes,” *Appl. Phys. Lett.*, vol. 79, no. 14, pp. 2258–2260, Oct. 2001, doi: 10.1063/1.1408274.
[84] A. Karkkanen, T. Avarmaa, and R. Jaaniso, “Gas Sensing Properties of SWCNT and Teflon AF Composites,” in *2007 IEEE SENSORS*, Oct. 2007, pp. 547–549. doi: 10.1109/ICSENS.2007.4388456.
[85] J. Li, D. Gu, Y. Yang, H. Du, and X. Li, “UV Light Activated $SnO_2$/ZnO Nanofibers for Gas Sensing at Room Temperature,” *Front. Mater.*, vol. 6, p. 158, Jul. 2019, doi: 10.3389/fmats.2019.00158.
[86] M. Rodner *et al.*, “Performance tuning of gas sensors based on epitaxial graphene on silicon carbide,” *Mater. Des.*, vol. 153, pp. 153–158, Sep. 2018, doi: 10.1016/j.matdes.2018.04.087.
[87] V. Dua *et al.*, “All-Organic Vapor Sensor Using Inkjet-Printed Reduced Graphene Oxide,” *Angew. Chem. Int. Ed.*, vol. 49, no. 12, pp. 2154–2157, Mar. 2010, doi: 10.1002/anie.200905089.
[88] X. Yan *et al.*, “High-Performance UV-Assisted $NO_2$ Sensor Based on Chemical Vapor Deposition Graphene at Room Temperature,” *ACS Omega*, vol. 4, no. 10, pp. 14179–14187, Sep. 2019, doi: 10.1021/acsomega.9b00935.
[89] J. Lin, J. Zhong, J. Reiber Kyle, M. Penchev, M. Ozkan, and C. S. Ozkan, “Molecular absorption and photodesorption in pristine and functionalized large-area graphene layers,” *Nanotechnology*, vol. 22, no. 35, p. 355701, Sep. 2011, doi: 10.1088/0957-4484/22/35/355701.
[90] S. Xu, L. Zhang, B. Wang, and R. S. Ruoff, “Chemical vapor deposition of graphene on thin-metal films,” *Cell Rep. Phys. Sci.*, vol. 2, no. 3, p. 100372, Mar. 2021, doi: 10.1016/j.xcrp.2021.100372.
[91] W. Fu, L. Jiang, E. P. van Geest, L. M. C. Lima, and G. F. Schneider, “Sensing at the Surface of Graphene Field-Effect Transistors,” *Adv. Mater.*, vol. 29, no. 6, p. 1603610, 2017, doi: 10.1002/adma.201603610.
[92] E. Cazalas, I. Childres, A. Majcher, T.-F. Chung, Y. P. Chen, and I. Jovanovic, “Hysteretic response of chemical vapor deposition graphene field effect transistors on SiC substrates,” *Appl. Phys. Lett.*, vol. 103, no. 5, p. 053123, Jul. 2013, doi: 10.1063/1.4816426.
[93] H. Li, X. Han, A. S. Childress, A. M. Rao, and G. Koley, “Investigation of carrier density and mobility variations in graphene caused by surface adsorbates,” *Phys. E Low-Dimens. Syst. Nanostructures*, vol. 107, pp. 96–100, Mar. 2019, doi: 10.1016/j.physe.2018.11.021.
[94] M. Gautam and A. H. Jayatissa, “Graphene based field effect transistor for the detection of ammonia,” *J. Appl. Phys.*, vol. 112, no. 6, p. 064304, Sep. 2012, doi: 10.1063/1.4752272.
[95] M. Nakamura, Y. Kanai, Y. Ohno, K. Maehashi, K. Inoue, and K. Matsumoto, “Graphene-FET-based gas sensor properties depending on substrate surface conditions,” *Jpn. J. Appl. Phys.*, vol. 54, no. 6S1, p. 06FF11, Jun. 2015, doi: 10.7567/JJAP.54.06FF11.

[96] A. Berholts, T. Kahro, A. Floren, H. Alles, and R. Jaaniso, “Photo-activated oxygen sensitivity of graphene at room temperature,” *Appl. Phys. Lett.*, vol. 105, no. 16, p. 163111, Oct. 2014, doi: 10.1063/1.4899276.

[97] N. Lu, L. Wang, L. Li, and M. Liu, “A review for compact model of graphene field-effect transistors,” *Chin. Phys. B*, vol. 26, no. 3, p. 036804, Mar. 2017, doi: 10.1088/1674-1056/26/3/036804.

[98] T. Hayasaka, Y. Kubota, Y. Liu, and L. Lin, “The influences of temperature, humidity, and $O_2$ on electrical properties of graphene FETs,” *Sens. Actuators B Chem.*, vol. 285, pp. 116–122, Apr. 2019, doi: 10.1016/j.snb.2019.01.037.

[99] P. Recum and T. Hirsch, “Graphene-based chemiresistive gas sensors,” *Nanoscale Adv.*, vol. 6, no. 1, pp. 11–31, 2024, doi: 10.1039/D3NA00423F.

[100] O. Leenaerts, B. Partoens, and F. M. Peeters, “Adsorption of $H_2O$, $NH_3$, CO, $NO_2$, and NO on graphene: A first-principles study,” *Phys. Rev. B*, vol. 77, no. 12, Mar. 2008, doi: 10.1103/PhysRevB.77.125416.

[101] J. Dai, J. Yuan, and P. Giannozzi, “Gas adsorption on graphene doped with B, N, Al, and S: A theoretical study,” *Appl. Phys. Lett.*, vol. 95, no. 23, p. 232105, Dec. 2009, doi: 10.1063/1.3272008.

[102] G. Lee, G. Yang, A. Cho, J. W. Han, and J. Kim, “Defect-engineered graphene chemical sensors with ultrahigh sensitivity,” *Phys. Chem. Chem. Phys.*, vol. 18, no. 21, pp. 14198–14204, 2016, doi: 10.1039/C5CP04422G.

[103] C. Gionco, A. Battiato, E. Vittone, M. C. Paganini, and E. Giamello, “Structural and spectroscopic properties of high temperature prepared $ZrO_2$–$TiO_2$ mixed oxides,” *J. Solid State Chem.*, vol. 201, pp. 222–228, May 2013, doi: 10.1016/j.jssc.2013.02.040.

[104] H. Chen, C. E. Nanayakkara, and V. H. Grassian, “Titanium Dioxide Photocatalysis in Atmospheric Chemistry,” *Chem. Rev.*, vol. 112, no. 11, pp. 5919–5948, Nov. 2012, doi: 10.1021/cr3002092.

[105] U. Diebold, “The surface science of titanium dioxide,” *Surf. Sci. Rep.*, vol. 48, no. 5–8, pp. 53–229, Jan. 2003, doi: 10.1016/S0167-5729(02)00100-0.

[106] J. Gaj *et al.*, “Metallurgical graphene under different gas atmospheres and UV radiation for gas-sensing applications,” *Sens. Actuators Phys.*, vol. 312, p. 112152, Sep. 2020, doi: 10.1016/j.sna.2020.112152.

[107] H. Hashtroudi *et al.*, “Hydrogen gas sensing properties of microwave-assisted 2D Hybrid Pd/rGO: Effect of temperature, humidity and UV illumination,” *Int. J. Hydrog. Energy*, vol. 46, no. 10, pp. 7653–7665, Feb. 2021, doi: 10.1016/j.ijhydene.2020.11.268.

[108] Á. Peña *et al.*, “Optimization of multilayer graphene-based gas sensors by ultraviolet photoactivation,” *Appl. Surf. Sci.*, vol. 610, p. 155393, Feb. 2023, doi: 10.1016/j.apsusc.2022.155393.

[109] K. F. Mak, L. Ju, F. Wang, and T. F. Heinz, “Optical spectroscopy of graphene: From the far infrared to the ultraviolet,” *Solid State Commun.*, vol. 152, no. 15, pp. 1341–1349, Aug. 2012, doi: 10.1016/j.ssc.2012.04.064.

[110] J. J. Jankowski, D. J. Kieber, and K. Mopper, “Nitrate and Nitrite Ultraviolet Actinometers,” *Photochem. Photobiol.*, vol. 70, no. 3, pp. 319–328, Sep. 1999, doi: 10.1111/j.1751-1097.1999.tb08143.x.

[111] S. Yu. Davydov and A. V. Zubov, “On the Dipole–Dipole Interaction of Atoms in the Layers Adsorbed on Three- and Two-Dimensional Semiconductors,” *Phys. Solid State*, vol. 62, no. 8, pp. 1469–1472, Aug. 2020, doi: 10.1134/S10637834 20080090.

[112] T. Sasaki, Y. Ebina, Y. Kitami, M. Watanabe, and T. Oikawa, “Two-Dimensional Diffraction of Molecular Nanosheet Crystallites of Titanium Oxide,” *J. Phys. Chem. B*, vol. 105, no. 26, pp. 6116–6121, Jul. 2001, doi: 10.1021/jp010421i.

[113] A. Falak *et al.*, “Simultaneous achievement of superior response and full recovery of titanium dioxide/graphene hybrid FET sensors for $NH_3$ through p- to n-mode switch,” *Phys. Chem. Chem. Phys.*, vol. 22, no. 29, pp. 16701–16711, 2020, doi: 10.1039/D0CP02070B.

# ORIGINAL PUBLICATIONS

# CURRICULUM VITAE


| | |
|---|---|
| Name: | Artjom Berholts |
| Date of Birth | 03.10.1989 |
| E-mail | artjom.berholts@ut.ee |


**Education:**

| | |
|---|---|
| 2013– | University of Tartu, doctoral studies, materials science |
| 2011–2013 | University of Tartu, master's studies, materials science |
| 2008–2011 | University of Tartu, bachelor's studies, materials science |

**Work experience:**

| | |
|---|---|
| 15.01.2020– | University of Tartu, Institute of Physics, Specialist |
| 01.09.2017–31.12.2019 | University of Tartu, Institute of Physics, Junior Research Fellow |
| 01.07.2013–28.02.2014 | University of Tartu, Institute of Physics, Engineer |

**Publications**:


**Berholts, A**., Kodu, M., Rubin, P., Kahro, T., Alles, H., Jaaniso, R. (2024), Layered Heterostructure of Graphene and $TiO_2$ as a Highly Sensitive and Stable Photoassisted $NO_2$ Sensor, *ACS Appl. Mater. Interfaces*, 16 (33), 43827–43837.

Kodu, M., **Berholts, A**., Kahro, T., Eriksson, J., Yakimova, R., Avarmaa, T., Renge, I., Alles, H., Jaaniso, R. (2019), Graphene-based ammonia sensors functionalised with sub-monolayer $V_2O_5$: a comparative study of chemical vapour deposited and epitaxial graphene, *Sensors*, 19, 951/1–17.

Kodu, M., **Berholts, A**., Kahro, T., Eriksson, J., Yakimova, R., Avarmaa, T., Renge, I., Alles, H., Jaaniso, R. (2018), Highly sensitive $NH_3$ sensors using CVD and epitaxial graphene functionalised with vanadium(V) oxide: a comparative study, *Proceedings*, 2, 854/1–5.

Eltermann, M., Kiisk, V., **Berholts, A**., Dolgov, L., Lange, S., Utt, K., Jaaniso, R. (2018), Modeling of luminescence-based oxygen sensing by redox-switched energy transfer in nanocrystalline $TiO_2$:$Sm^{3+}$, *Sensors and Actuators B Chemical*, 265, 556–564. DOI: 10.1016/j.snb.2018.03.034.

Kodu, M., **Berholts, A**., Kahro, T., Kook, M., Ritslaid, P., Seemen, H., Avarmaa, T., Alles, H., Jaaniso, R. (2017), Graphene functionalised by laser-ablated $V_2O_5$ for a highly sensitive $NH_3$ sensor, *Beilstein J. Nanotechnol.*, 8, 571–578.

Kodu, M., **Berholts, A**., Kahro, T., Avarmaa, T., Kasikov, A., Niilisk, A., Alles, H., Jaaniso R. (2016), Highly sensitive $NO_2$ sensors by pulsed laser deposition on graphene, *Appl. Phys. Lett.*, 109, 113108/1–5.

**Berholts, A**., Kahro, T., Floren, A., Alles, H., Jaaniso, R. (2014), Photo-activated oxygen sensitivity of graphene at room temperature, *Appl. Phys. Lett.*, 105, 163111/1–5.

**Conference presentations:**

Berholts, A., Kodu, M., Kahro, T., Renge, I., Avarmaa, T., Alles, H., Jaaniso, R., Graphene-based gas sensors modified by pulsed laser deposition for $NO_2$ and $NH_3$ detection. FMTDK Teaduskonverents, Tallinn, Estonia, June 2017.

Berholts, A., Kahro, T., Kodu, M., Avarmaa, T., Niilisk, A., Alles, H., Jaaniso, R., Functionalization of graphene by pulsed laser deposition: impact on gas sensitivity, Graphene Week 2015, Manchester, UK, 22–26 June 2015.

Berholts, A.; Kahro, T.; Floren, A.; Alles, H.; Jaaniso, R., Light-activated gas sensitivity of graphene in ambient conditions, Graphene Week 2014, Göteburg, Sweden, 23–27 June, 2014.

# ELULOOKIRJELDUS


| | |
|---|---|
| Nimi: | Artjom Berholts |
| Sünniaeg: | 03.10.1989 |
| E-mail: | artjom.berholts@ut.ee |


**Hariduskäik:**

| | |
|---|---|
| 2013– | Tartu Ülikool, doktoriõpe, materjaliteadus |
| 2011–2013 | Tartu Ülikool, magistriõpe, materjaliteadus |
| 2008–2011 | Tartu Ülikool, bakalaureuseõpe, materjaliteadus |

**Töökohad ja ametid:**

| | |
|---|---|
| 15.01.2020– | Tartu Ülikool, füüsika instituut, sensoorika spetsialist |
| 01.09.2017–31.12.2019 | Tartu Ülikool, füüsika instituut, materjaliteaduse nooremteadur |
| 01.07.2013–28.02.2014 | Tartu Ülikool, füüsika instituut, insener |

**Publikatsioonid**:


**Berholts, A**., Kodu, M., Rubin, P., Kahro, T., Alles, H., Jaaniso, R. (2024), Layered Heterostructure of Graphene and $TiO_2$ as a Highly Sensitive and Stable Photoassisted $NO_2$ Sensor, *ACS Appl. Mater. Interfaces*, 16 (33), 43827–43837.

Kodu, M., **Berholts, A**., Kahro, T., Eriksson, J., Yakimova, R., Avarmaa, T., Renge, I., Alles, H., Jaaniso, R. (2019), Graphene-based ammonia sensors functionalised with sub-monolayer $V_2O_5$: a comparative study of chemical vapour deposited and epitaxial graphene, *Sensors*, 19, 951/1–17.

Kodu, M., **Berholts, A**., Kahro, T., Eriksson, J., Yakimova, R., Avarmaa, T., Renge, I., Alles, H., Jaaniso, R. (2018), Highly sensitive $NH_3$ sensors using CVD and epitaxial graphene functionalised with vanadium(V) oxide: a comparative study, *Proceedings*, 2, 854/1–5.

Eltermann, M., Kiisk, V., **Berholts, A**., Dolgov, L., Lange, S., Utt, K., Jaaniso, R. (2018), Modeling of luminescence-based oxygen sensing by redox-switched energy transfer in nanocrystalline $TiO_2$:$Sm^{3+}$, *Sensors and Actuators B Chemical*, 265, 556–564. DOI: 10.1016/j.snb.2018.03.034.

Kodu, M., **Berholts, A**., Kahro, T., Kook, M., Ritslaid, P., Seemen, H., Avarmaa, T., Alles, H., Jaaniso, R. (2017), Graphene functionalised by laser-ablated $V_2O_5$ for a highly sensitive $NH_3$ sensor, *Beilstein J. Nanotechnol.*, 8, 571–578.

Kodu, M., **Berholts, A**., Kahro, T., Avarmaa, T., Kasikov, A., Niilisk, A., Alles, H., Jaaniso R. (2016), Highly sensitive $NO_2$ sensors by pulsed laser deposition on graphene, *Appl. Phys. Lett.*, 109, 113108/1–5.

**Berholts, A**., Kahro, T., Floren, A., Alles, H., Jaaniso, R. (2014), Photo-activated oxygen sensitivity of graphene at room temperature, *Appl. Phys. Lett.*, 105, 163111/1–5.

**Konverentsiettekanded**:

Berholts, A., Kodu, M., Kahro, T., Renge, I., Avarmaa, T., Alles, H., Jaaniso, R., Graphene-based gas sensors modified by pulsed laser deposition for $NO_2$ and $NH_3$ detection. FMTDK Teaduskonverents, Tallinn, Estonia, June 2017.

Berholts, A., Kahro, T., Kodu, M., Avarmaa, T., Niilisk, A., Alles, H., Jaaniso, R., Functionalization of graphene by pulsed laser deposition: impact on gas sensitivity, Graphene Week 2015, Manchester, UK, 22–26 June 2015.

Berholts, A.; Kahro, T.; Floren, A.; Alles, H.; Jaaniso, R., Light-activated gas sensitivity of graphene in ambient conditions, Graphene Week 2014, Göteburg, Sweden, 23–27 June, 2014.

# DISSERTATIONES SCIENTIAE MATERIALIS UNIVERSITATIS TARTUENSIS

1. **Martin Järvekülg**. Tubular microstructures by Hf-, Zr- and Ti-butoxide gel sheet rolling. Tartu, 2011, 112 p.
2. **Sergei Vlassov**. Investigation of nanoscale interactions and mechanical properties of nanostructures using quartz tuning fork based real-time measurements. Tartu, 2011, 171 p.
3. **Margus Kodu**. Pulsed Laser Deposition of Magnesium Oxide and Barium Ternary Oxides for Plasma Display Protective Layers. Tartu, 2011, 89 p.
4. **Rainer Pärna**. Surface studies of some oxide films. Tartu, 2011, 129 p.
5. **Jevgeni Šulga**. Self-assembly and interaction of nanostructures. Tartu, 2011, 114 p.
6. **Wojciech Kuznik**. Quantum-chemical computer simulations of the linear and non-linear optical properties of pyrazoloquinoline and dicyanopyrazine derivatives. Tartu, 2012, 89 p.
7. **Leonid Dorogin**. Structural and tribological properties of zero- and one-dimensional nanocrystals. Tartu, 2012, 193 p.
8. **Viljar Palmre**. Fabrication and characterization of microporous carbon-based electroactive polymer actuators. Tartu, 2012, 99 p.
9. **Madis Paalo**. Synthesis of CNT-metal oxide nanocomposites: sol-gel process, rheology, structural and functional properties. Tartu, 2014, 175 p.
10. **Raul Välbe**. Developement of ionic liquid composites by sol-gel method for elaboration of industrial nano- and microstructures. Tartu, 2014, 97 p.
11. **Urmas Joost**. Impurity and preparation dependent properties of titania thin films. Tartu, 2014, 155 p.
12. **Madis Umalas**. Application of sol-gel technology for production of ceramic nanocomposites and functional coatings. Tartu, 2015, 136 p.
13. **Elena Samsonova**. Energy transfer probe as a tool to study morphological and structural origins of fluorescence quenching in rare-earth doped nanophosphors. Tartu, 2015, 114 p.
14. **Jay Mondal**. Novel Corrosion Protective Nanostructured Composite Coatings. Tartu, 2016, 104 p.
15. **Kathriin Utt**. Metal oxide mesostructures for optical applications. Tartu, 2016, 88 p.
16. **Kaido Siimon**. Electrospun gelatin cross-linked by glucose. Tartu, 2016, 84 p.
17. **Marko Part**. Combined three-dimensional sol-gel structures and atomic layer deposited thin films. Tartu, 2017, 162 p.
18. **Pejman Rasti**. Analysis of Remote Sensing Image Super Resolution using Fluid Lenses. Tartu, 2017, 188 p.
19. **Ivo Romet**. Recombination luminescence of doped borates: origin and application prospects in dosimetry. Tartu, 2017, 111 p.

20. **Vladimir I. Kondratiev**. Processing and characterization of transparent electrode materials. Tartu, 2017, 111 p.
21. **Taivo Jõgiaas**. Mechanical properties of atomic layer deposited thin films and nanocomposites. Tartu, 2017, 125 p.
22. **Lauri Aarik**. Atomic layer deposition and characterization of thin oxide films for application in protective coatings. Tartu, 2017, 180 p.
23. **Triin Kangur**. Preparation and functional properties of stochastic micro-structured sol-gel silica materials. Tartu, 2018, 96 p.
24. **Marta Berholts**. Fragmentation of ionic and hydrogen-bonded molecules induced by synchrotron radiation. Tartu, 2018, 126 p.
25. **Priit Priimägi**. Development and optimization of 3D-microbatteries. Tartu, 2018, 118 p.
26. **Siim Hödemann**. Residual stress determination in chemically strengthened and thermally tempered glass plates using scattered light method. Tartu, 2019, 146 p.
27. **Jekaterina Kozlova**. Complex characterization of graphene structures on nanometer level. Tartu, 2019, 206 p.
28. **Kristjan Kalam**. Magnetic, electric and structural properties of atomic layer deposited zirconia-based nanolaminates and mixtures. Tartu, 2020, 94 p.
29. **Triinu Vihmann**. Ionic liquids: synthesis and application in lubrication and lithography. Tartu, 2020, 102 p.
30. **Helina Seemen**. Atomic layer deposition and microscopic analysis of magnetically and electrically polarizable thin solid films. Tartu, 2021, 126 p.
31. **Ekaterina Vagapova**. Fluorescence quenching in inorganic crystalline solids activated by neodymium ions; from bulk to micro- and nanocrystals. Tartu, 2021, 116 p.
32. **Evgenii Strugovshchikov**. First-principles studies on rare-earth metal-hydride-based smart materials. Tartu, 2021, 166 p.
33. **Maido Merisalu**. Nanostructured Coatings for Car and Aerospace Industries. Tartu, 2022, 179 p.
34. **Elena Vinogradova**. Optical centers and quantum entangled states of Nd3+ ions in doped fluoride crystals. Tartu, 2023, 92 p.
35. **Dmytro Danilian**. "Photocatalytic materials for water treatment and antimicrobial applications". Tartu, 2024, 139 p.
36. **Kristel Möls**. Metastable $TiO_2$-II in atomic layer deposited thin and ultrathin films: stabilization, properties and impact on film growth. Tartu, 2024, 112 p.
37. **Helle-Mai Piirsoo**. Mechanical Properties of Nanocomposites with Artificial Periodic Structure. Tartu, 2024, 144 p.